Numerical simulations of the Euler system with congestion constraint

Pierre Degond[*], Jiale Hua[†], Laurent Navoret[‡]

Abstract

In this paper, we study the numerical simulations for Euler system with maximal density constraint. This model is developed in [9, 17] with the constraint introduced into the system by a singular pressure law, which causes the transition of different asymptotic dynamics between different regions. To overcome these difficulties, we adapt and implement two asymptotic preserving (AP) schemes originally designed for low Mach number limit [16, 18] to our model. These schemes work for the different dynamics and capture the transitions well. Several numerical tests both in one dimensional and two dimensional cases are carried out for our schemes.

Key words: Finite volume scheme, Congestion, Asymptotic-Preserving schemes, All-speed flows, Pressureless Gas Dynamics

1 Introduction

Several models involve congestion constraints: concentration constraints occur in multi-phase flow modeling [12], maximal density constraints occur when dealing with finite-size interactive agents in herds of gregarious mammals [17], in cars or pedestrians flows [9, 10, 3], flux constraints occur for supply chains [2],... The dynamics in congested regions strongly differ from the dynamics dynamics in free regions. To study the transitions between congested and free regions, a general methodology was first carried out in [12] for multiphase flows and later on generalized to traffic [9] or herding problems [17]: the stiffness of the constraint leads to a singular perturbation problem and then the limit problem provides a clear cut-off between the two dynamics. In this paper, we will consider the Euler system with a singular pressure which encodes a maximal density constraint. As in [17], the limit problem is a two-phase model between

---

[*]Université de Toulouse; UPS, INSA, UT1, UTM; Institut de Mathématiques de Toulouse; F-31062 Toulouse, France. Email: pierre.degond@math.univ-toulouse.fr

[†]CNRS; Institut de Mathématiques de Toulouse UMR 5219; F-31062 Toulouse, France. Email: jiale.hua@math.univ-toulouse.fr

[‡]CNRS; Institut de Mathématiques de Toulouse UMR 5219; F-31062 Toulouse, France. Email: laurent.navoret@math.univ-toulouse.fr

incompressible regions, where the maximal density is reached, and compressible regions for lower densities. Our goal is to provide numerical schemes that are able to capture this limit problem and these transitions. In this paper, we adapt and compare two numerical methods presented in [18] and in [16] for the low Mach number limit.

A lot of efforts have been made to devise numerical schemes valid for all Mach numbers, that is, for both compressible and incompressible flows. They avoid the switch between different methods, when different Mach numbers occur in different sub-domains. Among such schemes, one approach is the extension of compressible conservative methods to incompressible flows thanks to precon- ditioning techniques [37, 20, 19, 28]. The second approach is the extension of incompressible methods to compressible flows and leads to pressure correction methods on staggered grids [21] and their conservative versions [33, 6, 38]. Their adaptation to the conservative frameworks has led to time semi-implicit schemes : the implicit discretization of the fluxes (the mass flux and the pressure part of the momentum flux are taken implicitly) is combined with the resolution of the elliptic equation satisfied by the pressure. The implicit treatment of the pressure flux ensures stability with respect to the propagation of fast acoustic waves in the low-Mach number limit but induces a lot of diffusion. We can cite numerous works following this methodology [25, 39, 30, 31, 34]. The methods we consider in this paper are among the simplest ones: the scheme in [18] is a semi-implicit scheme with a division of the pressure into explicit and implicit parts and in [16], the Gauge decomposition of the momentum enables the hy- drostatic pressure to act only on the divergence-free part of the momentum. The former method will be called in the present paper the Direct method, while the Gauge method will refer to the latter.

The purpose of this paper is to present simple variants of the Direct [18] and the Gauge method [16], that are able to handle congestion problems. As announced above, they are designed to solve the isentropic Euler system sup- plemented by a pressure law $p(\rho)$, which is singular as the density ρ approaches a maximal density denoted ρ^*. A small parameter ε is introduced to control the stiffness of this maximal density constraint: the rescaled pressure $\varepsilon p(\rho)$ is of order $O(1)$ in congested regions $\rho \sim \rho^*$ and of order $O(\varepsilon)$ in low density regions $\rho < \rho^*$. In the limit $\varepsilon \to 0$, the system leads to a two-phase model: the incompressible Euler system in maximal density domains and the pressure- less gas dynamics system for uncongested densities domains. This asymptotic model was first proposed and studied in [12, 8] in a one-dimensional framework. However, this asymptotic model is only partially defined since transmission conditions at the interfaces between the two phases are lacking. Besides, un- less one-dimensional solutions can be provided (see [12] and appendix A), their extensions to the two-dimensional case are open problems (especially the dynam- ics of two colliding congested domains). In this context, asymptotic preserving scheme is a good tool for this problem.

The Direct and the Gauge methods are called asymptotic-preserving (AP) since they are uniformly consistent with the low-Mach number limit. Besides, they are also uniformly stable. These methods are expected to capture both the

compressible and the incompressible dynamics arising in the congestion limit of the Euler system with the maximal density constraint. In this case, such AP numerical schemes are very powerful since they provide the dynamics of transitions, for which analytical results may be lacking. Moreover, they enable us to avoid dealing with physical and numerical interface tools, such as front-tracking [36] or volume-of-fluid methods [23]. Unlike these tracking methods, ours are front-capturing methods and then share some analogies with level-set [32] and diffusive interface methods [1]: like level-set method, the dynamics of the transition are implicitly embodied in the dynamics of an auxiliary function which here is the density and like the diffusive interface methods, the sharp interface is viewed as the limit of the smooth transitions of the perturbation problem.

The Direct method cannot be directly applied to the congestion problem. Indeed, in [18], the pressure $p(\rho)$ is splitted into an explicit part $p_0(\rho)$ and an implicit part $p_1(\rho)$ in order to keep some numerical diffusion and avoid numerical oscillations. For the singular congestion pressure-law, we modify this splitting, such that it still ensures the stability of the scheme. Besides, it ensures the consistency of the explicit part of the scheme with the limit pressureless gas dynamics in the low density regions. Indeed, the pressureless gas dynamics system is weakly hyperbolic and there is no uniqueness of the entropic solution [11]. Then, keeping an explicit pressure $p_0(\rho)$ makes the asymptotic numerical solutions consistent with the good entropic solutions. For the same reasons, this pressure splitting is introduced into the Gauge method.

The AP property of the two methods for the congested Euler system is demonstrated for the congested domains. This analysis is hard to extend to co-existent congested and uncongested regions since the dynamics of the interfaces between the different regions is not explicitly implemented into the schemes. However, several numerical test-cases provides numerical evidence of the AP property. Comparisons of the two schemes are also carried out and different behaviours of the schemes at the interfaces are measured.

The paper is organized as follows. In section 2, we introduce the Euler system with the maximal density constraint. To have some basic idea of the solution, we give its formal asymptotic limit. In section 3, we describe the time semi-discretization of the Direct and Gauge schemes. The fully space and time discretizations are exposed in section 4, in one dimensional setting: they are based on the centered Rusanov scheme, also called the local Lax-Friedrichs scheme [27]. The two dimensional setting is quite similar. Therefore, we present it in the appendix. Finally, numerical simulations are performed in section 5 to compare the two schemes: several test cases in the one dimensional setting and one case in the two dimensional setting. Two appendices close this study: we describe one-dimensional solutions and the two dimensional discretizations.

2   The Euler system with congestion and its asymptotic limit

2.1   The model

We consider the two-dimensional Euler system:

$$\partial_t \rho + \nabla_{\boldsymbol{x}} \cdot \boldsymbol{q} = 0, \tag{1}$$

$$\partial_t \boldsymbol{q} + \nabla_{\boldsymbol{x}} \cdot \left(\frac{\boldsymbol{q} \otimes \boldsymbol{q}}{\rho} \right) + \nabla_{\boldsymbol{x}} p(\rho) = 0, \tag{2}$$

where $\rho(\boldsymbol{x}, t) \in \mathbb{R}$ denotes the mass density, $\boldsymbol{q} = \rho \boldsymbol{u}(\boldsymbol{x}, t) \in \mathbb{R}^2$ is the momentum field depending on the position $\boldsymbol{x} \in \mathbb{R}^2$ and the time $t > 0$. The pressure $p(\rho)$ is an increasing function such that $p(\rho) \sim \rho^\gamma$ for densities $\rho \ll 1$ and $p(\rho) \to +\infty$ as ρ tends to the congestion density ρ^*. In the following, we will consider the function:

$$p(\rho) = \frac{1}{\left(\frac{1}{\rho} - \frac{1}{\rho^*} \right)^\gamma}, \quad \gamma > 0. \tag{3}$$

This pressure prevents the density from exceeding the congestion density. A variant is the van der Waals equation of state [22]. The operators $\nabla_{\boldsymbol{x}}$ and $\nabla_{\boldsymbol{x}}\cdot$ are the gradient and the divergence of vector fields or tensor. For two vectors $\boldsymbol{a}$ and $\boldsymbol{b}$, $\boldsymbol{a} \otimes \boldsymbol{b}$ denotes the tensor product.

This model already appears in [17] with the additional constraint: $\boldsymbol{q}/\rho = \boldsymbol{u} \in \mathbb{S}^1$. In this paper, we focus on the pressure singularity and the corresponding numerical schemes.

The singular pressure induces two different dynamics: for regions with densities near ρ^*, the pressure takes very large values in comparison with the pressure in low-density regions. As in [17] and previous work on traffic modeling [9], we would like to clearly separate the two different dynamics. To this aim, we rescale $p(\rho)$ into $\varepsilon p(\rho)$, where the parameter $\varepsilon \ll 1$ is the scale of the pressure in the low density regions: $p(\rho) = O(\varepsilon)$ for density $\rho \ll 1$ while $p(\rho) = O(1)$ for density $\rho \sim \rho^*$, see Fig. 1.

Denoting ρ^ε and $\boldsymbol{q}^\varepsilon$ the new unknowns, system (1)-(2) becomes:

$$\partial_t \rho^\varepsilon + \nabla_{\boldsymbol{x}} \cdot \boldsymbol{q}^\varepsilon = 0, \tag{4}$$

$$\partial_t \boldsymbol{q}^\varepsilon + \nabla_{\boldsymbol{x}} \cdot \left(\frac{\boldsymbol{q}^\varepsilon \otimes \boldsymbol{q}^\varepsilon}{\rho^\varepsilon} \right) + \nabla_{\boldsymbol{x}} \left(\varepsilon p(\rho^\varepsilon) \right) = 0, \tag{5}$$

Moreover, taking the time derivative of (4) and subtracting the divergence of equation (5), we easily obtain the wave-like equation satisfied by the density:

$$\partial_{t^2} \rho - \nabla_{\boldsymbol{x}}^2 : \left(\frac{\boldsymbol{q}^\varepsilon \otimes \boldsymbol{q}^\varepsilon}{\rho^\varepsilon} \right) - \Delta_{\boldsymbol{x}}(\varepsilon p(\rho^\varepsilon)) = 0,$$

where $\nabla_{\boldsymbol{x}}^2$ denotes the tensor of the second derivatives and for two tensors $\boldsymbol{a}$ and $\boldsymbol{b}$ and $\boldsymbol{a} : \boldsymbol{b}$ denotes the contracted product of tensor. The operator $\Delta_{\boldsymbol{x}}$
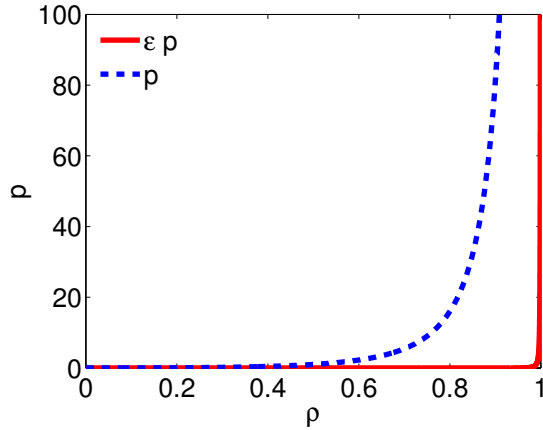
Figure 1: The pressure p and the rescaled pressure εp

denotes the Laplacian of a scalar function. Actually, system (4)-(5) is a strictly hyperbolic problem, with characteristic wave speeds in the x-direction (where x is the first component of a basis of $\mathbb{R}^2$) given by:

$$\lambda_1^\varepsilon = u_x^\varepsilon - \sqrt{\varepsilon p'(\rho^\varepsilon)}, \quad \lambda_2^\varepsilon = u_x^\varepsilon, \quad \lambda_3^\varepsilon = u_x^\varepsilon + \sqrt{\varepsilon p'(\rho^\varepsilon)}, \tag{6}$$

where u_x^ε is the x-component of the macroscopic velocity $\boldsymbol{u}^\varepsilon(x,t) = \boldsymbol{q}^\varepsilon(x,t)/\rho^\varepsilon(x,t)$. Standard hyperbolic numerical schemes have to resolve the Courant-Friedrichs-Levy (CFL) condition:

$$\max(|\lambda_1^\varepsilon|, |\lambda_2^\varepsilon|, |\lambda_3^\varepsilon|)\Delta t \le \Delta x. \tag{7}$$

In the next section, we will see that this constraint may be too stringent for these schemes to capture the asymptotic limit.

2.2 The asymptotic limit

The limit of the pressure term $\varepsilon p(\rho^\varepsilon)$ depends on the limit of ρ^ε. Indeed, if $\rho^\varepsilon \to \rho$ with $\rho < \rho^*$, then $\varepsilon p(\rho^\varepsilon)$ converges to 0. Otherwise, $\rho^\varepsilon \to \rho^*$ and the limit of $\varepsilon p(\rho^\varepsilon)$, denoted $\bar{p}$, can be non zero and depends on the convergence rate of ρ^ε. We assume that the limit $\bar{p}$ is always finite. Therefore, the formal limit of system (4)-(5) as ε goes to zero is:

$$\partial_t \rho + \nabla_{\boldsymbol{x}} \cdot \boldsymbol{q} = 0, \tag{8}$$

$$\partial_t \boldsymbol{q} + \nabla_{\boldsymbol{x}} \cdot \left(\frac{\boldsymbol{q} \otimes \boldsymbol{q}}{\rho} \right) + \nabla_{\boldsymbol{x}} \bar{p} = 0, \tag{9}$$

$$(\rho - \rho^*)\bar{p} = 0. \tag{10}$$

A one-dimensional version of this asymptotic model was proposed for two-phase flow modeling in [12], where the density plays the role of the volume fraction

of liquid in a liquid-gas model. The derivation of the model lies on a relaxation to zero of the relative velocities of the gas and liquid and is therefore different from the one studied in this article. Existence and stability of solutions are proved for the one-dimensional version of system (8)-(9)-(10) in [8], and in all dimensions with viscous term in [29].

As regards the characteristic speeds, we note that if $\varepsilon p(\rho^\varepsilon)$ tends to $\bar{p} < +\infty$, then we have $\rho^* - \rho^\varepsilon = O(\varepsilon^{\frac{1}{\gamma}})$ and then $\varepsilon p'(\rho^\varepsilon) = O(\varepsilon^{\frac{1}{\gamma}-1})$. Therefore, if $\gamma > 1$, $\lambda^\varepsilon_\pm$ can become infinite and waves with infinite speed can occur. It is the low-Mach number asymptotics that leads to incompressible dynamics. Actually, in the congested domain where $\rho = \rho^*$, system (8)-(9)-(10) yields the incompressible Euler equation:

$$
\begin{aligned}
&\rho = \rho^*, \\
&\nabla_{\boldsymbol{x}} \cdot \boldsymbol{u} = 0, \\
&\partial_t \boldsymbol{u} + \boldsymbol{u} \cdot \nabla_{\boldsymbol{x}} \boldsymbol{u} + \frac{1}{\rho^*} \nabla_{\boldsymbol{x}} \bar{p} = 0.
\end{aligned}
\tag{11}
$$

Equation (11) is the incompressible constraint and the Lagrange multiplier related to this constraint is the pressure $\bar{p}$. The CFL condition (7) degenerate into $\Delta t = 0$: standard hyperbolic schemes are unable to compute the asymptotic dynamics. Thus, numerical schemes with relaxed CFL condition have to be designed.

In the free domain where $\rho < \rho^*$, the CFL condition (7) is not an obstacle although the system degenerates into a non-hyperbolic problem: $\lim \lambda^\varepsilon_1 = \lim \lambda^\varepsilon_3 = u$. This is a large-Mach number asymptotic. Numerical schemes, originally developed for hyperbolic systems, have to be proved to capture this singular limit. System (8)-(9)-(10) yields the pressureless gas dynamics:

$$
\begin{aligned}
&\rho < \rho^*, \\
&\partial_t \rho + \nabla_{\boldsymbol{x}} \cdot \boldsymbol{q} = 0, \\
&\partial_t \boldsymbol{q} + \nabla_{\boldsymbol{x}} \cdot \left(\frac{\boldsymbol{q} \otimes \boldsymbol{q}}{\rho} \right) = 0,
\end{aligned}
$$

Without upper-bound on the density, this system would lead to concentration phenomena even for smooth initial data and so the density may become a measure with singular part. It is related to the so-called sticky particle dynamics. Existence of solutions and numerical schemes have been developed in the one-dimensional case [11, 14].

The asymptotic system (8)-(9)-(10) is not complete: the well-posed definition of $\bar{p}$ requires boundary conditions at the interface between congested regions $\{\rho = \rho^*\}$ and free regions $\{\rho < \rho^*\}$. They can not be directly obtained by the formal derivation. One possible answer to this question is to look at the theoretical asymptotic behaviour of solutions of the initial system (4)-(5). Such an approach is investigated in appendix A but only in the one-dimensional case. Extensions to two dimensional settings are difficult and will be the subject of future works. The second possible approach is to use numerical schemes to

capture the asymptotic dynamics: this is the main methodology we develop in this paper. It has the advantage to be applicable in any dimensions. However, one-dimensional problems are still good test cases to valid these numerical schemes.

3 Time semi-discretization schemes

This section is the center of this paper. It is dedicated to the presentation of two numerical schemes, which are able to capture the asymptotic limit of the Euler system with congestion presented in the previous section. For this purpose, we adapt the asymptotic-preserving (AP) schemes developed in [18] and [16] for the low-Mach limit of the isentropic Euler system.

3.1 The time semi-implicit discretization

We first define a time semi-implicit discretization, which will be the building block of the considered AP schemes.

Let ρ^n, q^n be the approximations of the density ρ and the momentum q at $t^n = n\Delta t, n = 0, 1, \ldots$, where Δt is the time step. The semi-discretization of the AP scheme for the n-th time step is as follows:

$$\frac{\rho^{n+1} - \rho^n}{\Delta t} + \nabla_{\boldsymbol{x}} \cdot \boldsymbol{q}^{n+1} = 0, \tag{12}$$

$$\frac{\boldsymbol{q}^{n+1} - \boldsymbol{q}^n}{\Delta t} + \nabla_{\boldsymbol{x}} \cdot \left(\frac{\boldsymbol{q}^n \otimes \boldsymbol{q}^n}{\rho^n} \right) + \nabla_{\boldsymbol{x}}(\varepsilon p(\rho^{n+1})) = 0. \tag{13}$$

The full discretization in time and space is postponed to the next section. We want to show that the scheme is asymptotic-preserving. In other words, it captures the correct behaviour of the limiting equation as $\varepsilon \to 0$. To achieve this, the implicitness of $\rho, \boldsymbol{q}$ is crucial.

Observe that the explicit part of the above scheme is pressureless. However, the pressureless Euler system is weakly hyperbolic, giving rise to the formation of density concentrations known as delta-shocks. Several numerical schemes for this system was proposed in [13, 26, 4, 7]. In [13], the authors proposed a kinetic scheme, that is valid for the isothermal Euler system and leads to a kinetic scheme for the pressureless system in the vanishing pressure limit. Here, to avoid this difficulty and as already proposed in [18], we split the pressure into an explicit and an implicit part. Numerical tests in section 5 will demonstrate how this splitting reduces oscillations. Thus, the scheme is written as follows:

$$\frac{\rho^{n+1} - \rho^n}{\Delta t} + \nabla_{\boldsymbol{x}} \cdot \boldsymbol{q}^{n+1} = 0, \tag{14}$$

$$\frac{\boldsymbol{q}^{n+1} - \boldsymbol{q}^n}{\Delta t} + \nabla_{\boldsymbol{x}} \cdot \left(\frac{\boldsymbol{q}^n \otimes \boldsymbol{q}^n}{\rho^n} \right) + \nabla_{\boldsymbol{x}}(\varepsilon p_0(\rho^n)) + \nabla_{\boldsymbol{x}}(\varepsilon p_1(\rho^{n+1})) = 0, \tag{15}$$
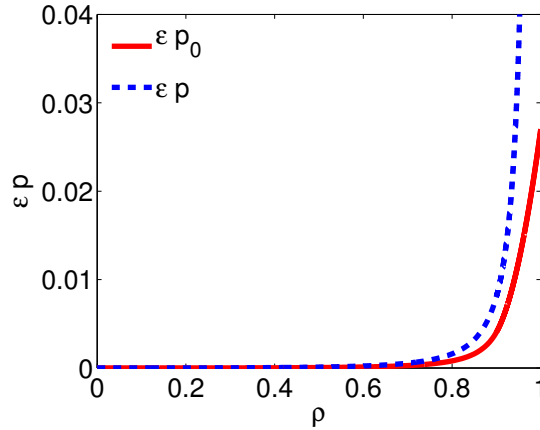
Figure 2: The plots of εp and εp_0 as functions of ρ with $\varepsilon = 10^{-4}, \gamma = 2$.

where the explicit part is given as

$$
p_0(\rho) = \begin{cases} \dfrac{1}{2}p(\rho), & \text{if } \rho \leq \rho_* - \delta, \\[2mm] \dfrac{1}{2}\Big(p(\rho_* - \delta) + p'(\rho_* - \delta)(\rho - \rho_* + \delta) \\[1mm] \quad + \dfrac{1}{2}p''(\rho_* - \delta)(\rho - \rho_* + \delta)^2\Big), & \text{if } \rho > \rho_* - \delta, \end{cases} \tag{16}
$$

and the implicit part is

$$
p_1(\rho) = p(\rho) - p_0(\rho), \quad \delta = \varepsilon^{\frac{1}{\gamma+2}}. \tag{17}
$$

The choice of δ makes sure that p_0 and its derivatives up to second order are always bounded. To make sure all the coefficients appearing in the elliptic equation we will derive in the next section are continuous, we choose p_0 to be a second order approximation to p, instead of a first order one. For later usage, also note that the function $p_1(\rho)$ is invertible. This is easily seen from the property of function p and p_0, see Fig 2. By the definition, the Courant-Friedrich-Lewy (CFL) condition for the explicit part is

$$
\Delta t \leq \frac{\sigma \Delta x}{\max\{|\frac{q}{\rho}| + \sqrt{\varepsilon p_0'(\rho)}\}}, \tag{18}
$$

where σ is the Courant number. Since $\varepsilon p_0'$ is always bounded, the CFL condition can be satisfied uniformly in ε.

8

3.2 The Direct method

To get the solution, we will rewrite the above scheme into another form. By inserting (15) into (14), we can get an elliptic equation for ρ:

$$\frac{\rho^{n+1} - \rho^n}{\Delta t} + \nabla_{\boldsymbol{x}} \cdot \boldsymbol{q}^n - \Delta t \Delta_{\boldsymbol{x}} (\varepsilon p_1(\rho^{n+1})) - \Delta t \nabla^2_{\boldsymbol{x}} : \left(\frac{\boldsymbol{q}^n \otimes \boldsymbol{q}^n}{\rho^n} \right) - \Delta t \Delta_{\boldsymbol{x}} (\varepsilon p_0(\rho^n)) = 0. \tag{19}$$

From this equation, we can solve ρ^{n+1}. However, if we solve ρ directly, the density constraint $\rho \leq \rho^*$ may not be satisfied due to discretization errors. Thus, we write $\rho^{n+1} = \rho(p_1^{n+1})$ in (19) and solve the equation in terms of p_1. The density constraint $\rho \leq \rho^*$ will be automatically satisfied. Moreover, the positivity of ρ can be ensured by the fact that the discretized equation satisfies the maximal principle.

Once ρ^{n+1} is obtained, we can obtain $\boldsymbol{q}^{n+1}$ from (15) easily.

$$\boldsymbol{q}^{n+1} = \boldsymbol{q}^n - \Delta t \left\{ \nabla_{\boldsymbol{x}} \cdot \left(\frac{\boldsymbol{q}^n \otimes \boldsymbol{q}^n}{\rho^n} \right) + \nabla_{\boldsymbol{x}} (\varepsilon p_0(\rho^n)) + \nabla_{\boldsymbol{x}} (\varepsilon p_1(\rho^{n+1})) \right\}. \tag{20}$$

Remark 1 *In the numerical simulation, we can also improve the accuracy by implementing a fully implicit scheme, which iterates the above scheme to solve (14) and (15) with $\frac{\boldsymbol{q} \otimes \boldsymbol{q}}{\rho}$ implicit. Suppose $\rho^{n+1,0} = \rho^n$ and $\boldsymbol{q}^{n+1,0} = \boldsymbol{q}^n$ and $\rho^{n+1,k}$, $\boldsymbol{q}^{n+1,k}$ are the solutions to the following equations.*

$$\frac{\rho^{n+1,k+1} - \rho^n}{\Delta t} + \nabla_{\boldsymbol{x}} \cdot \boldsymbol{q}^n - \Delta t \Delta_{\boldsymbol{x}} (\varepsilon p_1(\rho^{n+1,k+1}))$$

$$- \Delta t \, \nabla^2_{\boldsymbol{x}} : \left(\frac{\boldsymbol{q}^{n+1,k} \otimes \boldsymbol{q}^{n+1,k}}{\rho^{n+1,k}} \right) + \Delta_{\boldsymbol{x}} (\varepsilon p_0(\rho^n)) = 0, \tag{21}$$

$$\boldsymbol{q}^{n+1,k+1} = \boldsymbol{q}^n - \Delta t \left\{ \nabla_{\boldsymbol{x}} \left(\frac{\boldsymbol{q}^{n+1,k} \otimes \boldsymbol{q}^{n+1,k}}{\rho^{n+1,k}} \right) + \nabla_{\boldsymbol{x}} (\varepsilon p_0(\rho^n)) + \nabla_{\boldsymbol{x}} (\varepsilon p_1(\rho^{n+1,k+1})) \right\}. \tag{22}$$

As $k \to \infty$, the solution approximates to the one solving the fully implicit scheme (both in ρ and $\frac{\boldsymbol{q} \otimes \boldsymbol{q}}{\rho}$). This modification provides little improvement compared to the additional computational cost.

3.3 The Gauge method

Another way to implement the AP scheme is the Gauge method developed in [16]. It can be obtained by applying the Gauge decomposition

$$\boldsymbol{q} = \boldsymbol{a} - \nabla_{\boldsymbol{x}} \varphi, \quad \nabla_{\boldsymbol{x}} \cdot \boldsymbol{a} = 0 \tag{23}$$

where $\boldsymbol{a}$ is the incompressible part of field $\boldsymbol{q}$ and φ is the irrotational one. This decomposition is expected to be more robust for capturing incompressibility

constraint. We will see that it is partially right. By including this decomposition into equations (14) and (15), we get

$$\frac{\rho^{n+1} - \rho^n}{\Delta t} + \nabla_{\boldsymbol{x}} \cdot \boldsymbol{q}^n - \Delta t \Delta_{\boldsymbol{x}}(\varepsilon p_1(\rho^{n+1}))$$
$$- \Delta t \nabla_{\boldsymbol{x}}^2 : \left(\frac{\boldsymbol{q}^n \otimes \boldsymbol{q}^n}{\rho^n} \right) - \Delta t \Delta_{\boldsymbol{x}}(\varepsilon p_0(\rho^n)) = 0, \tag{24}$$

$$\Delta_{\boldsymbol{x}} \varphi^{n+1} = \frac{1}{\Delta t}(\rho^{n+1} - \rho^n), \tag{25}$$

$$\Delta_{\boldsymbol{x}} P^{n+1} = -\nabla_{\boldsymbol{x}}^2 : \left(\frac{\boldsymbol{q}^n \otimes \boldsymbol{q}^n}{\rho^n} \right) - \Delta_{\boldsymbol{x}}(\varepsilon p_0(\rho^n)), \tag{26}$$

$$\frac{\boldsymbol{a}^{n+1} - \boldsymbol{a}^n}{\Delta t} + \nabla_{\boldsymbol{x}} \cdot \left(\frac{\boldsymbol{q}^n \otimes \boldsymbol{q}^n}{\rho^n} \right) + \nabla_{\boldsymbol{x}}(\varepsilon p_0(\rho^n)) + \nabla_{\boldsymbol{x}} P^{n+1} = 0, \tag{27}$$

$$\boldsymbol{q}^{n+1} = \boldsymbol{a}^{n+1} - \nabla_{\boldsymbol{x}} \varphi^{n+1}. \tag{28}$$

Indeed, the equation (24) for p_1^{n+1} is derived from (14) and (15) similarly as in the Direct method. The Laplace equation (25) for φ^{n+1} is the direct consequence of applying the decomposition (28) and $\nabla_{\boldsymbol{x}} \cdot \boldsymbol{a}^{n+1} = 0$ to the density equation (14). The equation (26) for P^{n+1} and the equation (27) for $\boldsymbol{a}^{n+1}$ are obtained by inserting (28) and $\nabla_{\boldsymbol{x}} \cdot \boldsymbol{a}^{n+1} = \nabla_{\boldsymbol{x}} \cdot \boldsymbol{a}^n = 0$ into the momentum equation (15). Here a new unknown P is introduced, which is defined by

$$P^{n+1} = \varepsilon p_1(\rho^{n+1}) - \frac{\varphi^{n+1} - \varphi^n}{\Delta t}, \tag{29}$$

since (24)-(25) and (27) imply (15).

The original equations (14) and (15) can also be recovered from (24)-(28) by assuming $\nabla_{\boldsymbol{x}} \cdot \boldsymbol{a}^n = 0$. In fact, the equations for P^{n+1} and $\boldsymbol{a}^{n+1}$ ((26)-(27)) and $\nabla_{\boldsymbol{x}} \cdot \boldsymbol{a}^n = 0$ imply $\nabla_{\boldsymbol{x}} \cdot \boldsymbol{a}^{n+1} = 0$. This leads to the density equation (14) from the φ^{n+1} equation (25) and the decomposition (28). (14) combined with the p_1^{n+1} equation (24) will then allow us to recover the momentum equation (15).

The boundary conditions By solving the equations (24)-(28) in sequential order, we can update the value of $\rho, \boldsymbol{q}$. To do this, we need to provide boundary conditions for the Laplace equations for φ and P. The boundary conditions for P^{n+1} are somehow straightforward due to the implicit relation (29), once φ is known. And in solving φ^{n+1}, we may impose Dirichlet boundary condition on φ^{n+1} as follows:

$$\varphi^{n+1}|_\Omega = 0. \tag{30}$$

Indeed, other non-homogeneous Dirichlet boundary conditions can be chosen. This makes the unknown φ^{n+1} determined up to a linear function in space. However, this uncertainty can be removed by redefining $\boldsymbol{a}^{n+1}$. So we can always impose the homogeneous Dirichlet boundary conditions.

Simplification in the one dimensional case Observe that in the one dimensional case, $\nabla_{\boldsymbol{x}} \cdot a = 0$ implies that a is independent of x. We may thus rewrite (26) and (27) into a simpler equation by using (29)

$$a^{n+1} = a^n - \frac{\Delta t}{c-b} \left(\frac{(q^n)^2}{\rho^n} + \varepsilon p_0(\rho^n) + \varepsilon p_1(\rho^{n+1}) \right) \bigg|_b^c + \frac{1}{c-b} \left(\varphi^{n+1}|_b^c - \varphi^n|_b^c \right),$$

(31)

where the space-domain is $[b, c]$ and $f|_b^c = f(c) - f(b)$. This equation can be further simplified, since we impose the homogeneous Dirichlet boundary condition on φ all the time. This lead to

$$a^{n+1} = a^n - \frac{\Delta t}{c-b} \left(\frac{(q^n)^2}{\rho^n} + \varepsilon p_0(\rho^n) + \varepsilon p_1(\rho^{n+1}) \right) \bigg|_b^c.$$

(32)

With this reformulation, in the one dimensional case, we can reduce the number of elliptic equations to be solved to one and update the space independent variable a more efficiently. Also as a consequence of (30), a^n should be defined as the average of q^n.

$$a^n = \frac{1}{c-b} \int_b^c q^n dx.$$

(33)

In summary, the Gauge method in the one dimensional case is implemented through equations (24), (25), (28) and (32).

3.4   Discussion of the AP property

As for the AP property of the scheme, we give a formal proof. To be precise, we want to show that the system (19) and (15) becomes the incompressible Euler system as $\varepsilon \to 0$ in the congested region.

However, in contrast with the low Mach number limit of the isentropic Euler equation discussed in [18] or [16], the singularity in our model is embedded in the definition of p. New congestion regions may arise from non-congested ones. And by the analysis in section A, there is the possibility that $\rho^\varepsilon \to \rho^*$ but the limit of the pressure $\varepsilon p_1(\rho^\varepsilon) \to 0$ as $\varepsilon \to 0$. This means that although the congestion density is reached, there is no real congestion in this region. So it seems better to characterize the congestion region by defining $\bar{p} = \lim_{\varepsilon \to 0} \varepsilon p_1(\rho^\varepsilon) > 0$.

Currently, we can only show that in regions where both $\bar{p}^{n+1} = \lim_{\varepsilon \to 0} \varepsilon p_1((\rho^{n+1})^\varepsilon) > 0$ and $\bar{p}^n = \lim_{\varepsilon \to 0} \varepsilon p_1((\rho^n)^\varepsilon) > 0$, (19) and (20) tend to the incompressible Euler system as $\varepsilon \to 0$. The assumption $\bar{p}^{n+1} = \lim_{\varepsilon \to 0} \varepsilon p_1((\rho^{n+1})^\varepsilon) > 0$ is somehow essential given that declustering wave may appear in our model, since the pressure $\bar{p}$ can change from positive value to 0 instantaneously due to a declustering wave. The assumption $\bar{p}^n = \lim_{\varepsilon \to 0} \varepsilon p_1((\rho^n)^\varepsilon) > 0$ is also needed in case of the appearance of new congestion regions. In regions where $\bar{p}^{n+1} > 0$ and $\bar{p}^n > 0$, we have naturally that $(\rho^{n+1})^\varepsilon \to \rho^*$ and $(\rho^n)^\varepsilon \to \rho^*$ as $\varepsilon \to 0$. Taking the divergence of (20) and using (19), we can indeed recover (14), which

leads to the incompressibility of $(\boldsymbol{q}^{n+1})^\varepsilon$: $\nabla_{\boldsymbol{x}} \cdot (\boldsymbol{q}^{n+1})^{n+1} = 0$. Here the implicitness in (14) is crucial. Then (11) follows. Although we can only prove the AP property inside a congestion region, the numerical solutions provide evidence that the scheme is globally AP, including at transition between compressible and incompressible region.

As for the Gauge method, it is also AP since it is a direct consequence of (14) and (15).

In the numerical simulations, we will check the AP property for concrete test cases.

4   Full time and space discretization

In this section, we present the one dimensional full time and space discretization. The two dimensional discretization is the easy extension of the one dimensional case. For the sake of completeness, we include it in the appendix.

The Direct method: In the following, we consider the domain $[b, c] = [0, 1]$. Let the uniform spatial mesh be $\Delta x = \frac{1}{M}$, where M is a positive integer. Denote by $U_j^{n+1} = (\rho_j^n, q_j^n)^T$ the approximations of $U = (\rho, q)^T$ at time $t^n = n\Delta t$ and positions $x_j = j\Delta x$, for $j = 0, 1, \ldots, M$. We fully discretize the scheme (14) and (15) in the spirit of a local Lax-Friedrichs (or Rusanov) method [27] as follows:

$$\frac{\rho_j^{n+1} - \rho_j^n}{\Delta t} + \frac{1}{\Delta x}\left[Q_{j+1/2}(U_j^n, U_{j+1}^n, U_j^{n+1}, U_{j+1}^{n+1})\right.$$
$$\left. - Q_{j-1/2}(U_{j-1}^n, U_j^n, U_{j-1}^{n+1}, U_j^{n+1})\right] = 0, \tag{34}$$

$$\frac{q_j^{n+1} - q_j^n}{\Delta t} + \frac{1}{\Delta x}\left[F_{j+1/2}(U_j^n, U_{j+1}^n) - F_{j-1/2}(U_{j-1}^n, U_j^n)\right]$$
$$+ \frac{1}{2\Delta x}\left[\varepsilon p_1(\rho_{j+1}^{n+1}) - \varepsilon p_1(\rho_{j-1}^{n+1})\right] = 0. \tag{35}$$

where the fluxes are given by:

$$Q_{j+1/2}^{n+1/2} = \frac{1}{2}\left[q_j^{n+1} + q_{j+1}^{n+1}\right] - \frac{1}{2}C_{j+1/2}^n(\rho_{j+1}^n - \rho_j^n), \tag{36}$$

$$F_{j+1/2}^n = \frac{1}{2}\left[\frac{(q_j^n)^2}{\rho_j^n} + \frac{(q_{j+1}^n)^2}{\rho_{j+1}^n} + \varepsilon p_0(\rho_{j+1}^n) + \varepsilon p_0(\rho_j^n)\right] - \frac{1}{2}C_{j+1/2}^n(q_{j+1}^n - q_j^n). \tag{37}$$

They consist of the sum of a centered flux, implicit in (36) , explicit in (37) and biased terms introducing diffusion. The quantity $C_{j+1/2}^n$ is the local diffusion coefficient and is given by:

$$C_{j+1/2}^n = \max\left\{\left|\frac{q_j^n}{\rho_j^n}\right| + \sqrt{\varepsilon p_0'(\rho_j^n)}, \left|\frac{q_{j+1}^n}{\rho_{j+1}^n}\right| + \sqrt{\varepsilon p_0'(\rho_{j+1}^n)}\right\}. \tag{38}$$

It is defined as the local maximal characteristic speed related to the explicit pressure p_0. Therefore, it remains bounded as ε goes to zero. The quantity $C^n_{j+1/2}$ provides a numerical viscosity which is needed for scheme stability. We note that only the central discretization part of the flux is taken implicit, while the numerical viscosity part is kept explicit. In the momentum flux, only the part of the flux which relates to pressure is taken implicit.

Based on this discretization, we can apply the same strategy as described in section 3.2 to get an elliptic equation in ρ by substituting (35) into (34):

$$
\frac{\rho^{n+1}_j - \rho^n_j}{\Delta t} + \frac{q^n_{j+1} - q^n_{j-1}}{2\Delta x} - \frac{\Delta t}{4\Delta x^2} \left[\varepsilon p_1(\rho^{n+1}_{j+2}) - 2\varepsilon p_1(\rho^{n+1}_j) + \varepsilon p_1(\rho^{n+1}_{j-2}) \right]
$$
$$
- \frac{1}{2\Delta x} \left[C_{j+1/2}(\rho^n_{j+1} - \rho^n_j) - C_{j-1/2}(\rho^n_j - \rho^n_{j-1}) \right] \tag{39}
$$
$$
- \frac{\Delta t}{2\Delta x^2} \left[F^n_{j+3/2} - F^n_{j+1/2} - F^n_{j-1/2} + F^n_{j-3/2} \right] = 0.
$$

This equation is consistent with equation (19) of the Direct method. Then we get a nonlinear equation for p_1:

$$
\rho((p_1)^{n+1}_j) - \frac{\Delta t^2}{4\Delta x^2} \left[\varepsilon(p_1)^{n+1}_{j+2} - 2\varepsilon(p_1)^{n+1}_j + \varepsilon(p_1)^{n+1}_{j-2} \right]
$$
$$
= \rho^n_j - \frac{\Delta t}{2\Delta x}(q^n_{j+1} - q^n_{j-1}) + \frac{\Delta t}{2\Delta x} \left[C_{j+1/2}(\rho^n_{j+1} - \rho^n_j) - C_{j-1/2}(\rho^n_j - \rho^n_{j-1}) \right]
$$
$$
+ \frac{\Delta t^2}{2\Delta x^2} \left[F^n_{j+3/2} - F^n_{j+1/2} - F^n_{j-1/2} + F^n_{j-3/2} \right].
$$
$$\tag{40}$$

As mentioned before, we will use Newton iterations to solve this nonlinear equation and get p^{n+1}_1. The density ρ^{n+1} is then obtained by inverting the nonlinear function $p_1 = p_1(\rho)$ with another Newton iteration. Once ρ^{n+1} is solved, q^{n+1} can be obtained by

$$
q^{n+1}_j = \Phi(U^n_{j-1}, U^n_j, U^n_{j+1}) - \frac{\Delta t}{2\Delta x} \left[\varepsilon p_1(\rho^{n+1}_{j+1}) - \varepsilon p_1(\rho^{n+1}_{j-1}) \right], \tag{41}
$$

with

$$
\Phi(U^n_{j-1}, U^n_j, U^n_{j+1}) = q^n_j - \frac{\Delta t}{\Delta x} \left[F^n_{j+1/2} - F^n_{j-1/2} \right]. \tag{42}
$$

The Gauge method Also based on (34) and (35), we can have the full time-space discretization of the Gauge method. Indeed, for the Gauge method, we need to discretize (40). This leads to

$$
\frac{1}{4\Delta x^2} \left[\varphi^{n+1}_{j+2} - 2\varphi^{n+1}_j + \varphi^{n+1}_{j-2} \right] =
$$
$$
\frac{1}{\Delta t}(\rho^{n+1}_j - \rho^n_j) - \frac{1}{2\Delta x} \left[C_{j+1/2}(\rho^n_{j+1} - \rho^n_j) - C_{j-1/2}(\rho^n_j - \rho^n_{j-1}) \right], \tag{43}
$$
$$
a^{n+1} = a^n - \Delta t \left(\frac{(q^n \otimes q^n)}{\rho^n} + \varepsilon p_0(\rho^n) + \varepsilon p_1(\rho^{n+1}) \right) \Big|^1_0
$$

$$+ \frac{\Delta t}{2} \sum_{1}^{M} \left[C_{j+1/2}(q_{j+1}^n - q_j^n) - C_{j-1/2}(q_j^n - q_{j-1}^n) \right], \tag{44}$$

$$q_j^{n+1} = a^{n+1} - \frac{1}{2\Delta x}(\varphi_{j+1}^{n+1} - \varphi_{j-1}^{n+1}). \tag{45}$$

The above equations are the direct consequences of (24)-(25), (28) and (32). However, in the numerical simulation, we will mainly test the schemes with (43) replaced by

$$\frac{1}{\Delta x^2} \left[\varphi_{j+1}^{n+1} - 2\varphi_j^{n+1} + \varphi_{j-1}^{n+1} \right] = \frac{1}{\Delta t}(\rho_j^{n+1} - \rho_j^n)$$
$$- \frac{1}{2\Delta x} \left[C_{j+1/2}(\rho_{j+1}^n - \rho_j^n) - C_{j-1/2}(\rho_j^n - \rho_{j-1}^n) \right], \tag{46}$$

which may be justified as being the direct discretization of (25) with some numerical viscosity added to the right hand side. The stencils are different in two cases. We call the Gauge method with stencil (43) *Gauge 2* method and the one with stencil (46) *Gauge 1* method, since they use grids $\varphi_{j\pm2}$ and $\varphi_{j\pm1}$ respectively in addition to φ_j. There is a big difference in performance between the two discretizations. In fact, we will see in the next section that the Gauge 2 method (with (43)) yields almost the same numerical result as the Direct method, while the Gauge 1 method (with (46)) performs quite differently from the Direct method. This may be partially due to the fact that the Gauge 1 method introduces more diffusion than the Gauge 2 method, which can be seen by inserting the Taylor expansion of $\varphi_{j\pm1}^{n+1}, \varphi_{j\pm2}^{n+1}$ around $x = j\Delta x$ into the discretizations:

$$\left(-\frac{1}{\Delta x^2} \left[\varphi_{j+1}^{n+1} - 2\varphi_j^{n+1} + \varphi_{j-1}^{n+1} \right] \right) - \left(-\frac{1}{4\Delta x^2} \left[\varphi_{j+2}^{n+1} - 2\varphi_j^{n+1} + \varphi_{j-2}^{n+1} \right] \right)$$
$$= \frac{1}{4} \frac{d^4}{dx^4} \varphi^{n+1}(j\Delta x)\Delta x^2 + O(\Delta x^4).$$

Numerical diffusion An important issue about the scheme is the numerical diffusion. From the equation (40), it can be seen that the diffusion for ρ is of the order of

$$\left(\frac{1}{2}(|u^n| + \sqrt{\varepsilon p_0'(\rho^n)})\Delta x + \Delta t \varepsilon p_1'(\rho^n) \right) \Delta_{\boldsymbol{x}} \rho^n + \Delta t \Delta_{\boldsymbol{x}}(\rho^n u^n \otimes u^n). \tag{47}$$

And similarly, by inserting (34) into the pressure p_1 term in (35) we can see that the diffusion for q is of the order of

$$\left(\frac{1}{2}(|u^n| + \sqrt{\varepsilon p_0'(\rho^n)}) \right) \Delta x \Delta_x q^n + \Delta t \varepsilon p_1'(\rho^n)\Delta_x q^n. \tag{48}$$

To damp out the oscillations in the mass and momentum equations, the required numerical diffusion is [27]

$$\left(\frac{1}{2}(|u^n| + \sqrt{\varepsilon p'(\rho^n)}) \right) \Delta x \Delta_x \rho^n, \left(\frac{1}{2}(|u^n| + \sqrt{\varepsilon p'(\rho^n)}) \right) \Delta x \Delta_x q^n, \tag{49}$$

respectively. To ensure that this numerical diffusion is achieved, we need the condition

$$\left(\frac{1}{2}(|u^n| + \sqrt{\varepsilon p_0'(\rho^n)})\Delta x + \varepsilon p_1'(\rho^n)\Delta t\right) \geq \left(\frac{1}{2}(|u^n| + \sqrt{\varepsilon p'(\rho^n)})\right)\Delta x, \quad (50)$$

which leads to

$$\frac{\Delta t}{\Delta x} \geq \frac{1}{2\left(\sqrt{\varepsilon p_0'(\rho^n)} + \sqrt{\varepsilon p'(\rho^n)}\right)}. \quad (51)$$

This condition is automatically satisfied in the congested region $(\rho \to \rho^*)$ for small ε, since $\varepsilon p'(\rho^n) \to \infty$ as $\varepsilon \to 0$. However, it contradicts the CFL condition in the non-congested region for small ε, since $\varepsilon p'(\rho^n)$ and $\varepsilon p_0'(\rho^n) \to 0$ as $\varepsilon \to 0$. From this analysis, there should be no oscillations in the congestion region while the numerical diffusion may not be sufficient in the non-congested region. However, numerical simulation seems to indicate that the numerical viscosity in this scheme is sufficient to damp out the oscillations in the non-congested region.

5 Numerical results

5.1 One dimensional test cases

In this section, we use several numerical examples to test the performance of the schemes. Corresponding to different situations, four examples are tested. All these examples are the compositions of Riemann problems. Since the exact solutions to Riemann problem can be determined as in section 2, we can compare the exact and numerical solutions. Different measurements of the relative errors will be applied to test the performance of our schemes. And the numerical Courant number is computed.

In the following, we choose $\gamma = 2$ and the maximal density $\rho^* = 1$. The test problems are:

$$(P1) : (\rho, q)(x, 0) = \begin{cases} (0.7, 0.8), & x \in [0, 0.5), \\ (0.7, -0.8), & x \in (0.5, 1], \end{cases} \quad (52)$$

$$(P2) : (\rho, q)(x, 0) = \begin{cases} (0.7, -0.8), & x \in [0, 0.5), \\ (0.7, 0.8), & x \in (0.5, 1], \end{cases} \quad (53)$$

$$(P3) : (\rho, q)(x, 0) = \begin{cases} (0.7, 0.8), & x \in [0, 0.25), \\ (0.8, -0.3), & x \in (0.25, 0.75), \\ (0.7, -1.2), & x \in (0.75, 1], \end{cases} \quad (54)$$

$$(P4) : (\rho, q)(x, 0) = \begin{cases} (0.8, 0.3), & x \in [0, 0.5), \\ (0.5, 0.1), & x \in (0.5, 1], \end{cases} \quad (55)$$
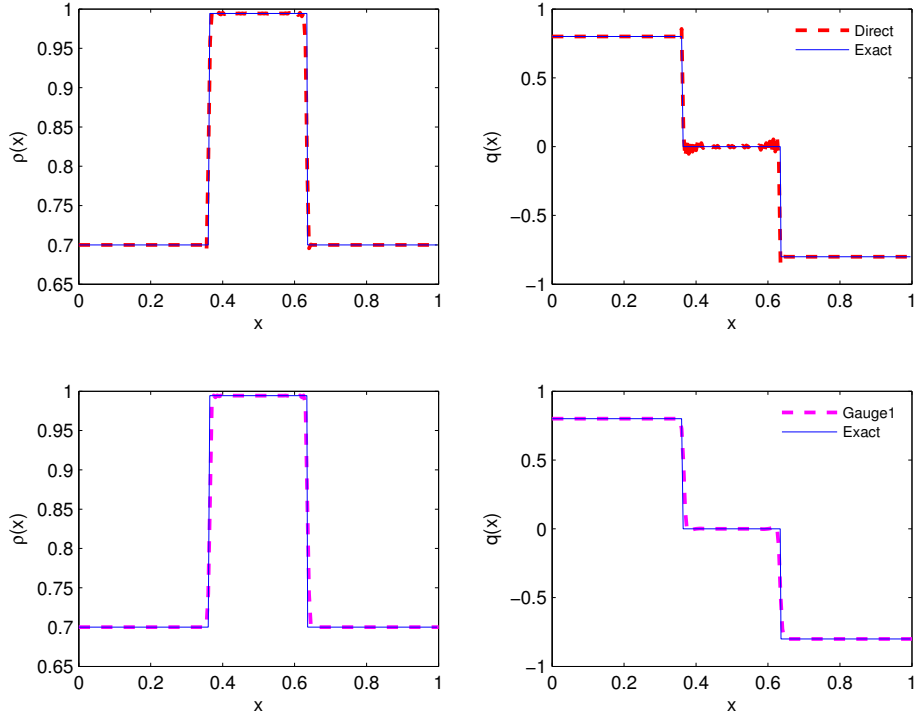
Figure 3: The direct and Gauge 1 methods for problem (P1) at $t = 0.05$ with $\varepsilon = 10^{-4}, \Delta x = 5 \times 10^{-3}, \Delta t = 5 \times 10^{-4}$. The solid lines are the exact solutions. The dashed curves are the numerical solutions. The left graphs are for ρ, the right ones for q, both as functions of x.

The first example ($P1$) illustrates how the AP schemes capture shocks near congestion. The second example ($P2$) shows how the AP schemes work near vacuum. The third example ($P3$) simulates the interaction of two shocks near congestion. The last example ($P4$) shows some problems in the Gauge 1 method and will be used to justify the splitting of p.

Example 1. The solution to the Riemann problem ($P1$) consists of two shocks propagating in the opposite directions. The density of the intermediate state is close to the maximal density. In the following, we will test the two methods described in section 4 with different parameters ε and different mesh sizes $\Delta x, \Delta t$.

1. First, we choose $\varepsilon = 10^{-4}, \Delta x = 5 \times 10^{-3}, \Delta t = 5 \times 10^{-4}$. We will compare the performances of the two methods proposed in section 4. It can be seen from Figure 3 that there is large oscillations of the momentum in the congested region. But the propagation of the shock is captured well. In comparison, the Gauge 1 method as illustrated in Figure 3 eliminates
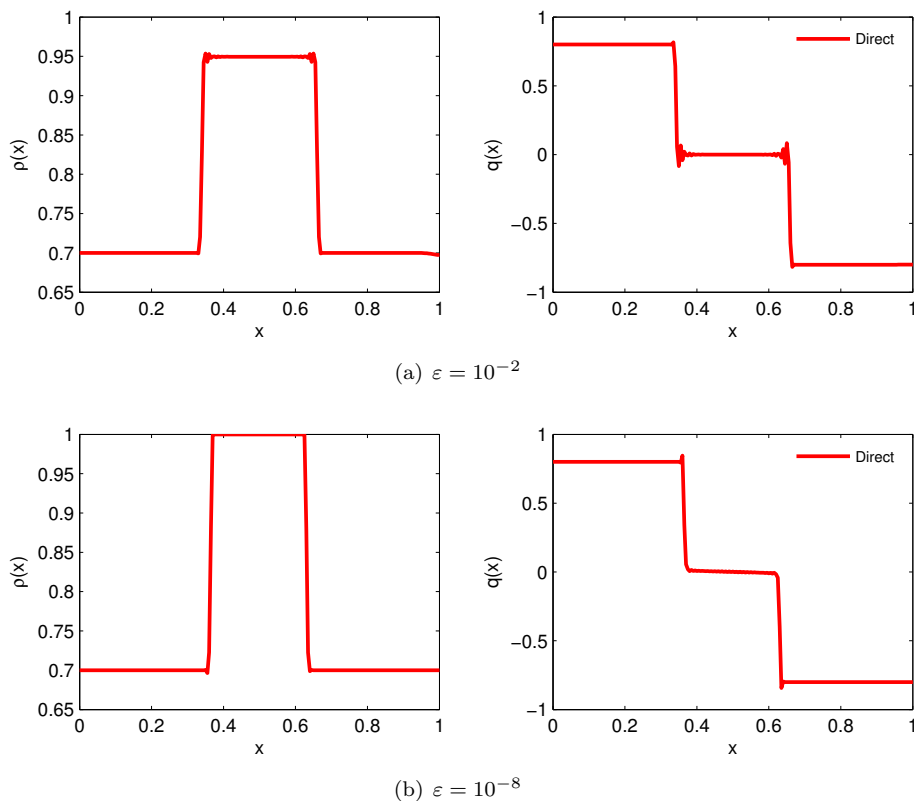
Figure 4: Fix $\Delta x = 5 \times 10^{-3}, \Delta t = 5 \times 10^{-4}$. The numerical results of the Direct method for problem (P1) at $t = 0.05$ with $\varepsilon = 10^{-2}$ and $\varepsilon = 10^{-8}$. The left graphs are for ρ, the right ones for q, both as functions of x.

all the oscillation.

2. We look how the choices of the parameters ε Δx and Δt affect the numerical result. We may fix $\Delta x, \Delta t$ but change the value of ε so as to test the cases $\varepsilon < \Delta t$ and $\varepsilon > \Delta t$. From the numerical results, it can be seen that the oscillations in the momentum always appear for different choices of ε but are smaller as $\varepsilon \to 0$ for this choice of parameter. This verifies the AP property. As for the Gauge 1 method, it has the same performance for all value of ε. Thus it shares the same property.

3. The above observation can be quantitatively investigated by measuring the difference between the numerical solution W and the theoretical one w. We use two measurements: one is the relative error of the numerical solution W compared with w in the sense of L^1 norm and the other is the

17

Parameters			Direct		Gauge 1	
ε	Δx	Δt	$e(W)$	ratio	$e(W)$	ratio
	1/200	1/250	1.1012×10^{-2}	-	1.1209×10^{-2}	-
	1/200	1/500	8.0103×10^{-3}	1.3747	7.8670×10^{-3}	1.4248
	1/200	1/1000	4.2631×10^{-3}	1.8790	4.9486×10^{-3}	1.5897
	1/200	1/2000	5.1528×10^{-3}	0.8273	5.4107×10^{-3}	0.9146
10^{-4}	1/200	1/10000	5.6843×10^{-3}	0.9065	1.5761×10^{-2}	0.3433
	1/200	1/1000	4.2631×10^{-3}	-	4.9486×10^{-3}	-
	1/400	1/2000	3.5612×10^{-3}	1.1971	3.1706×10^{-3}	1.5608
	1/800	1/4000	1.3085×10^{-3}	2.7216	1.4253×10^{-3}	2.2245
	1/1600	1/8000	5.7676×10^{-4}	2.2687	6.1850×10^{-4}	2.3044
	1/1600	1/16000	7.2302×10^{-4}	0.79771	7.0713×10^{-4}	0.87466
	1/200	1/250	1.3188×10^{-2}	-	1.3721×10^{-2}	-
	1/200	1/500	7.7490×10^{-3}	1.7019	8.5433×10^{-3}	1.6061
	1/200	1/1000	7.6793×10^{-3}	1.0091	7.8588×10^{-3}	1.0871
	1/200	1/2000	8.2751×10^{-3}	0.9280	7.5447×10^{-3}	1.0416
10^{-2}	1/200	1/10000	1.0758×10^{-2}	0.7692	1.5761×10^{-2}	0.4787
	1/200	1/1000	7.6793×10^{-3}	-	7.8588×10^{-3}	-
	1/400	1/2000	3.7602×10^{-3}	2.0423	3.8637×10^{-3}	2.0340
	1/800	1/4000	1.7934×10^{-3}	2.0967	1.8646×10^{-3}	2.0721
	1/1600	1/8000	8.0483×10^{-4}	2.2283	8.7074×10^{-4}	2.1414
	1/1600	1/16000	7.9308×10^{-4}	1.0148	8.4647×10^{-4}	1.0287

Table 1: Comparison of the L^1 relative error between the Direct and Gauge 1 methods at $t = 0.025$. The 'ratio' column ratio provides comparisons of the relative L^1 norm error between the previous and current rows, where either Δx is fixed or $\Delta x/\Delta t$ is fixed.

difference of their total variation:

$$e(W) = \frac{\|W - w\|_{L^1}}{\|w\|_{L^1}}, \text{ where } \|w\|_{L^1} = \frac{1}{M}\sum_j |w_j|, \tag{56}$$

$$g(W) = \frac{|\text{Tot. Var.}\{W\} - \text{Tot. Var.}\{w\}|}{\text{Tot. Var.}\{w\}}, \text{ where } \text{Tot. Var.}\{w\} = \sum_j |w_{j+1} - w_j|. \tag{57}$$

In Table 1 and 2, the relative error in terms of L^1 distance and total variation between the numerical and exact solutions at $t = 0.025$ are computed. The Gauge 2 method yields quite similar result to the Direct method. So it is not listed in the table. It can be seen that the Direct method is usually better than the Gauge 1 method in the L^1 norm. To reflect the observation we made from looking at Figure 3, we use the

Parameters			Direct		Gauge 1	
ε	Δx	Δt	$g(W)$	ratio	$g(W)$	ratio
10^{-4}	1/200	1/250	7.4909×10^{-3}	-	7.2225×10^{-4}	-
	1/200	1/500	7.5636×10^{-2}	0.0990	6.7956×10^{-3}	0.1063
	1/200	1/1000	4.1433×10^{-1}	0.1826	2.4506×10^{-2}	0.2773
	1/200	1/2000	8.5937×10^{-1}	0.4821	1.4766×10^{-2}	1.6596
	1/200	1/10000	1.0603	0.8105	1.8995×10^{-2}	0.7774
	1/200	1/1000	4.1433×10^{-1}	-	2.4506×10^{-2}	-
	1/400	1/2000	4.0126×10^{-1}	1.0326	3.8585×10^{-2}	0.6351
	1/800	1/4000	2.5996×10^{-1}	1.5435	2.4447×10^{-2}	1.5783
	1/1600	1/8000	5.4191×10^{-1}	0.4797	2.3520×10^{-2}	1.0394
	1/1600	1/16000	1.0294	0.5264	1.3054×10^{-2}	1.8017
10^{-2}	1/200	1/250	5.1377×10^{-5}	-	4.1271×10^{-4}	-
	1/200	1/500	5.2584×10^{-3}	0.0098	2.1808×10^{-4}	1.8925
	1/200	1/1000	1.1354×10^{-1}	0.0463	2.8711×10^{-3}	0.0760
	1/200	1/2000	4.9598×10^{-1}	0.2289	9.9861×10^{-3}	0.2875
	1/200	1/10000	1.2766	0.3885	4.4336×10^{-3}	2.2524
	1/200	1/1000	1.1354×10^{-1}	-	2.8711×10^{-3}	-
	1/400	1/2000	1.1856×10^{-1}	0.9577	2.9617×10^{-3}	0.9694
	1/800	1/4000	1.2408×10^{-1}	0.9555	2.9916×10^{-3}	0.9900
	1/1600	1/8000	1.2200×10^{-1}	1.0170	2.7207×10^{-3}	1.0996
	1/1600	1/16000	3.9234×10^{-1}	0.3110	1.3249×10^{-2}	0.2054

Table 2: Comparison of the total variation relative error between the Direct and Gauge 1 methods at $t = 0.025$. The 'ratio' column provides comparisons of the total variation relative error $g(W)$ between the previous and current rows, where either Δx is fixed or $\Delta x/\Delta t$ is fixed.

ε	Δx	stable Δt	$\max \lambda$	$(\max \lambda)\frac{\Delta t}{\Delta x}$
10^{-4}	$1/100$	$1/100$	1.2186	1.2186
10^{-4}	$1/200$	$1/210$	1.2669	1.2066
10^{-4}	$1/400$	$1/430$	1.1962	1.1128
10^{-4}	$1/800$	$1/870$	1.1962	1.1000
10^{-4}	$1/1600$	$1/1730$	1.1938	1.1041
10^{-2}	$1/100$	$1/100$	1.7903	1.4902
10^{-2}	$1/200$	$1/280$	1.6571	1.1836
10^{-2}	$1/400$	$1/580$	1.6486	1.1370
10^{-2}	$1/800$	$1/1170$	1.6486	1.1272
10^{-2}	$1/1600$	$1/2340$	1.6645	1.1381

Table 3: The numerical Courant number for the Direct method. $\max \lambda$ is the maximal eigenvalue of the explicit part of the scheme for all time steps before the waves reach the boundary.

total variation norm, which captures the oscillations better. For the total variation measurement, it can be seen that the Gauge 1 method is always better in controlling the oscillations. Another observation can be made from the tables is how the accuracy is changed with different parameters. For both two measurements, we test the accuracy with Δx fixed or $\Delta x/\Delta t$ fixed. In the test where Δx is fixed, it can also be seen that the relative error in L^1 norm can not be reduced much by refining the time mesh from $1/500$ to $1/10000$ with fixed $\Delta x = 1/200$. This feature is the same as the standard hyperbolic solvers: better accuracy can not be obtained by using a smaller Δt once the scheme is stable. In the test where $\Delta x/\Delta t$ is fixed, we check how the relative error is decreasing with respect to Δx. It is interesting to see that the error is not always decreasing. And since the convergence order for explicit local Lax-Friedrichs scheme with discontinuities is $\frac{1}{2}$ [27], we may expect that the relative error in L^1 norm is reduced by $\sqrt{2}$ when the space mesh is refined by 2 with $\Delta x/\Delta t$ fixed. However, this is not the case.

4. We will also check the numerical Courant number in tables 3 and 4. It can be seen that the CFL condition of our scheme is greatly improved from the one for standard hyperbolic solver $\Delta t = O(\varepsilon \Delta x)$.

5. We can also quantify the observation as in Figure 4. In Table 5, the relative errors of solutions in the L^1 norm or total variation are summarized. The data for $\varepsilon = 10^{-2}, 10^{-4}$ are the same as those in Table 1 and 2. It can be seen that there is no big increase in the relative error for different ε with fixed $\Delta x, \Delta t$. As discussed in section A, the theoretical solutions to system (62) and (63) with positive ε are converging to the solutions to systems with $\varepsilon = 0$ when $\varepsilon \to 0$. Thus, the numerical solutions tend to the theoretical solutions systems with $\varepsilon = 0$ for fixed $\Delta x, \Delta t$ as well. This

ε	Δx	stable Δt	max λ	max $\lambda\frac{\Delta t}{\Delta x}$
10^{-4}	1/100	1/100	1.2151	1.2151
10^{-4}	1/200	1/210	1.2279	1.1695
10^{-4}	1/400	1/500	1.3482	1.0786
10^{-4}	1/800	1/1340	1.4398	0.8596
10^{-4}	1/1600	1/3130	1.3555	0.69293
10^{-2}	1/100	1/100	1.6480	1.6480
10^{-2}	1/200	1/260	1.6475	1.2673
10^{-2}	1/400	1/540	1.6475	1.2204
10^{-2}	1/800	1/1190	1.6530	1.1112
10^{-2}	1/1600	1/2520	1.6490	1.0470

Table 4: The numerical Courant number for the Gauge 1 method. max λ is the maximal eigenvalue of the explicit part of the scheme for all time steps before the waves reach the boundary.

versifies the AP property.

6. With a slightly variant version of this test case, we can also see the role played by the splitting of pressure p. By making the momentum of the left and right states 10 times smaller, we have another test case $(P1')$ sharing the similar behaviour of $(P1)$.

$$(P1') : (\rho, q)(x, 0) = \begin{cases} (0.7, 0.08), & x \in [0, 0.5), \\ (0.7, -0.08), & x \in (0.5, 1], \end{cases} \tag{58}$$

In Figure 5, the numerical solutions obtained by the Direct method with and without p_0 are compared. This confirms the observation made in [18] for the low Mach number limit. It can be seen that a lot of extra oscillations appear in the numerical solutions when there is no splitting of pressure p ($p_0 = 0, p_1 = p$). That is the reason why we should add a p_0 term in the explicit part of the numerical scheme.

Example 2. The Riemann problem $(P2)$ is obtained by exchanging the left and right states of Riemann problem $(P1)$. So the solution to the problem $(P2)$ consists of two rarefaction waves and a vacuum state appears as the intermediate state. As shown in proposition 4, these two rarefaction waves tend to be contact waves.

As in example 1, We choose $\varepsilon = 10^{-4}, \Delta x = 5 \times 10^{-3}, \Delta t = 5 \times 10^{-4}$. t=0.0005. It can be seen from Figure 6 that the Direct method captures the vacuum and rarefaction waves well. In comparison, the Gauge 1 method as illustrated in Figure 6 shows larger diffusion.

Example 3. The solution to the problem $(P3)$ consists of two Riemann problems: both of them are like the Riemann problem in (P1). So there are two congested regions and eventually they will collide. We are interested in observing
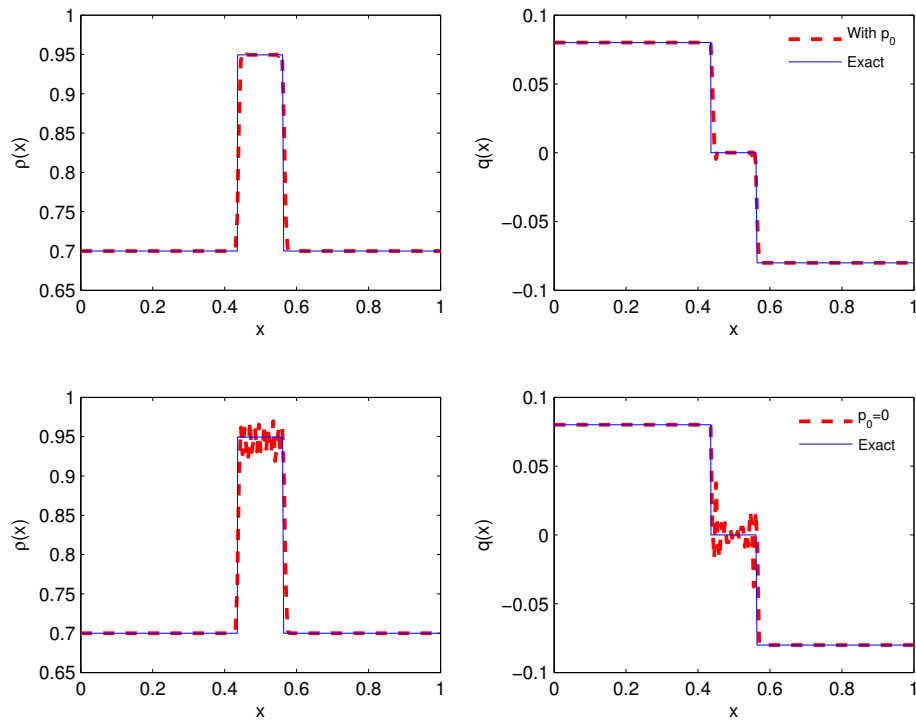
Figure 5: The numerical results of the Direct method with and without p_0 for problem (P1') at $t = 0.2$ with $\varepsilon = 10^{-4}, \Delta x = 5 \times 10^{-3}, \Delta t = 5 \times 10^{-4}$. The solid lines are the exact solutions. The dashed curves are the numerical solutions. The left graphs are for ρ, the right ones for q, both as functions of x.
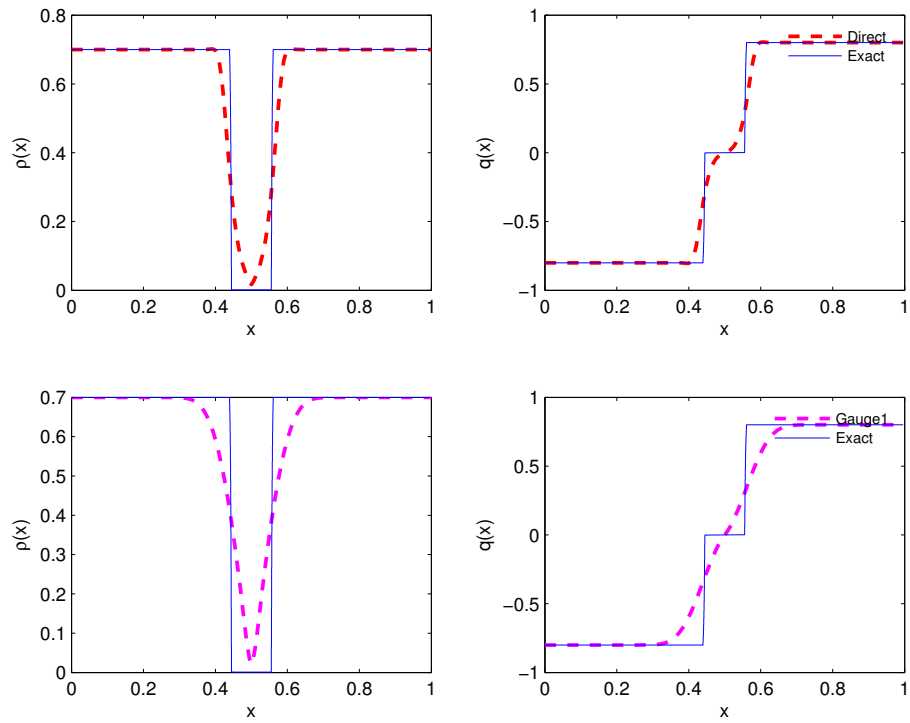
Figure 6: The Direct and Gauge 1 methods for problem (P2) at $t = 0.05$ with $\varepsilon = 10^{-4}, \Delta x = 5 \times 10^{-3}, \Delta t = 5 \times 10^{-4}$. The solid lines are the exact solutions. The dashed curves are the numerical solutions. The left graphs are for ρ, the right ones for q, both as functions of x.

Parameters			Direct		Gauge 1	
ε	Δx	Δt	$e(W)$	$g(W)$	$e(W)$	$g(W)$
	1/200	1/1000	7.6793×10^{-3}	1.1354×10^{-1}	7.8588×10^{-3}	2.8711×10^{-3}
	1/200	1/2000	8.2751×10^{-3}	4.9598×10^{-1}	7.5447×10^{-3}	9.9861×10^{-3}
10^{-2}	1/800	1/4000	1.7934×10^{-3}	1.2408×10^{-1}	1.8646×10^{-3}	2.9916×10^{-3}
	1/1600	1/16000	7.9308×10^{-4}	3.9234×10^{-1}	8.4647×10^{-4}	1.3249×10^{-2}
	1/200	1/1000	4.2631×10^{-3}	4.1433×10^{-1}	4.9486×10^{-3}	2.4506×10^{-2}
	1/200	1/2000	5.1528×10^{-3}	8.5937×10^{-1}	5.4107×10^{-3}	1.4766×10^{-2}
10^{-4}	1/800	1/4000	1.3085×10^{-3}	2.5996×10^{-1}	1.4253×10^{-3}	2.4447×10^{-2}
	1/1600	1/16000	7.2302×10^{-4}	1.0294	7.0713×10^{-4}	1.3054×10^{-2}
	1/200	1/1000	7.0600×10^{-3}	6.4521×10^{-1}	5.8159×10^{-3}	1.4861×10^{-2}
	1/200	1/2000	5.8872×10^{-3}	6.4091×10^{-3}	5.8872×10^{-3}	6.4091×10^{-3}
10^{-8}	1/800	1/4000	1.7611×10^{-3}	6.7218×10^{-1}	1.4624×10^{-3}	1.5544×10^{-2}
	1/1600	1/16000	9.1296×10^{-4}	8.2410×10^{-1}	8.0587×10^{-4}	1.6092×10^{-2}

Table 5: The L^1 and total variation relative error of the Direct and Gauge 1 methods at $t = 0.025$ for different ε.

how the numerical methods behave at collision. We fix $\Delta x = 5 \times 10^{-3}, \Delta t = 5 \times 10^{-4}$ and choose $\varepsilon = 10^{-4}$ and 10^{-8}. Since only shocks are involved, we will use the Gauge 1 method only.

From Figures 7 and 8, as ε becomes smaller, it takes shorter time to form a new congestion region from the two colliding congestion regions: from 48 time steps to no more than one time step. It can be seen that as $\varepsilon \to 0$, the collision of these two congested shocks aggregate instantaneously.

Example 4. The solution to the Riemann problem ($P4$) consists of two shocks with intermediate state away from the congestion density. So in the second Riemann problem there are two rarefaction waves and a vacuum state appears as the intermediate state. As shown in section 2, these two rarefaction waves tend to be contact waves.

As above, we choose $\varepsilon = 10^{-4}, \Delta x = 5 \times 10^{-3}, \Delta t = 5 \times 10^{-4}$. It can be seen from Figure 9 that the Direct method performs well when the density is far away from congestion. However, the Gauge 1 method does not work well possibly due to the extra diffusion.

Remark 2 *All the features described above are preserved when we apply the fully implicit method* (21)(22)*(implicit in both ρ and $\frac{q \otimes q}{\rho}$) to the Direct and Gauge 1 method. There is a little improvement in the accuracy but no major one.*

Finally, we can compare the Gauge 1 and Gauge 2 methods. With the stencil of (46) in the same setting as that of example 2, the Gauge 2 method yields almost the same numerical result as the Direct method (see Fig. 10).
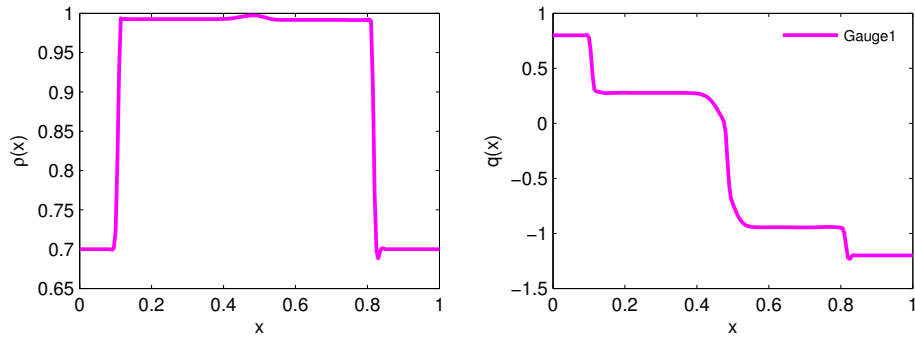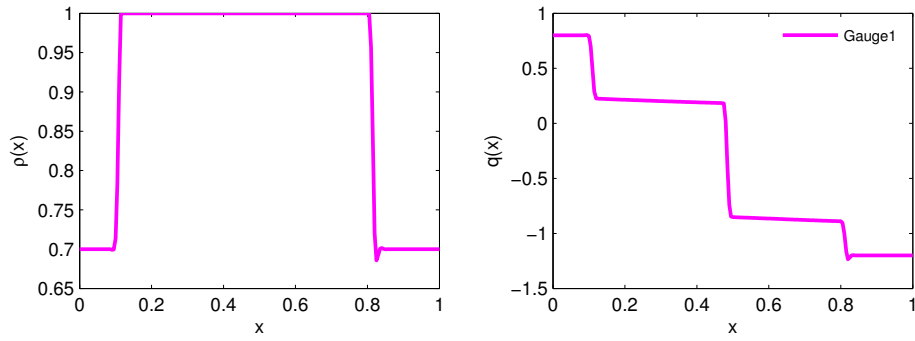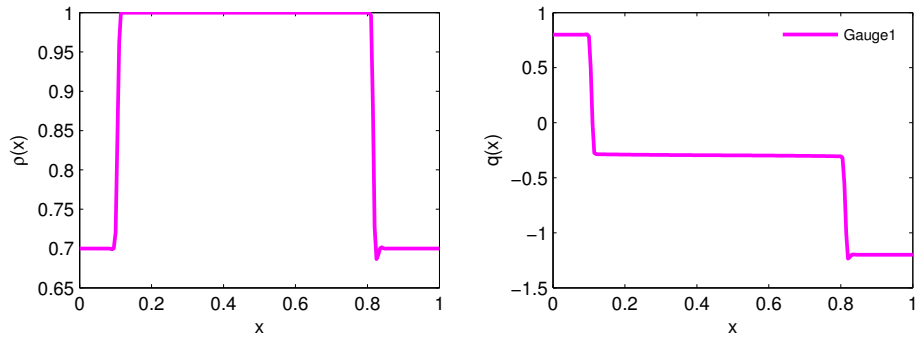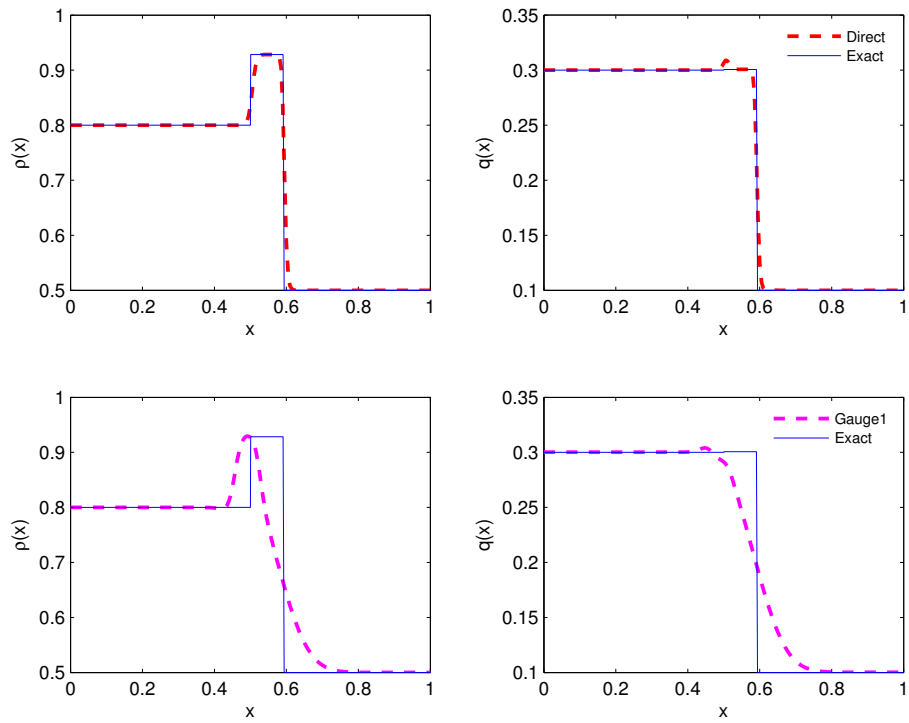
(a) $t = 0.0790$
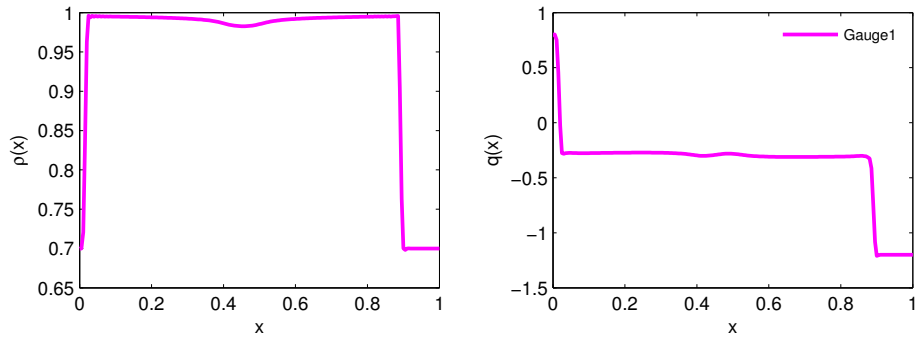
(b) $t = 0.1030$

Figure 7: Gauge 1 method for problem (P3) with $\varepsilon = 10^{-4}, \Delta x = 5 \times 10^{-3}, \Delta t = 5 \times 10^{-4}$. The left graphs are for ρ, the right ones for q, both as functions of x.

(a) $t = 0.0810$

(b) $t = 0.0815$

Figure 8: Gauge 1 method for problem (P3) with $\varepsilon = 10^{-8}, \Delta x = 5 \times 10^{-3}, \Delta t = 5 \times 10^{-4}$. The left graphs are for ρ, the right ones for q, both as functions of x.

26

Figure 9: The Direct and Gauge 1 methods for problem (P4) at $t = 0.2$ with $\varepsilon = 10^{-4}, \Delta x = 5 \times 10^{-3}, \Delta t = 5 \times 10^{-4}$. The solid lines are the exact solutions. The dashed curves are the numerical solutions. The left graphs are for ρ, the right ones for q, both as functions of x.
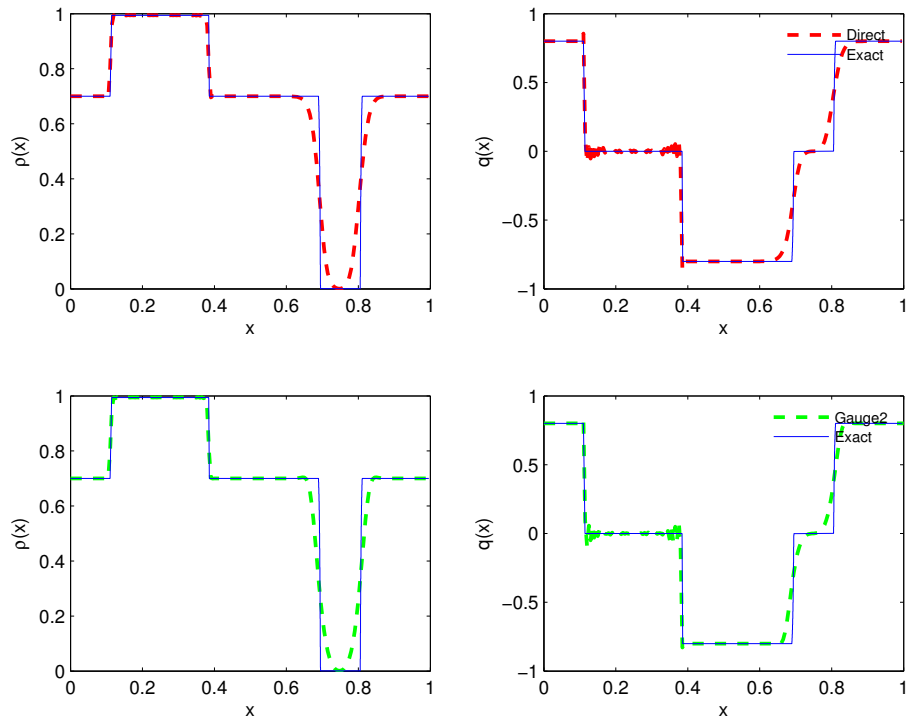
Figure 10: The Direct and Gauge 2 methods with discretization (43) for problem
(P2) at $t = 0.05$. The solid lines are the exact solutions. The dashed curves are
the numerical solutions. The left graphs are for ρ, the right ones for q, both as
functions of x.

5.2 A two dimensional test case

In this section, we will test the Direct and Gauge 1 method in the 2D case. Since there is no theoretical solution in 2D case, only some phenomena will be presented.

The test example is chosen to illustrate the collision of two congested regions. It is basically a two dimensional extension of the test case (P3) with some lateral shift. The initial data of the density and velocity is:

$$\rho = 0.8 \times 1_{A \cup B} + 0.6 \times 1_{[0,1] \times [0,1] \setminus (A \cup B)}, \tag{59}$$

$$\boldsymbol{q}(x, y, 0) = \begin{pmatrix} 1 \\ 0 \end{pmatrix} 1_A + \begin{pmatrix} -1 \\ 0 \end{pmatrix} 1_B, \tag{60}$$

$$A = \left[\frac{1}{6}, \frac{5}{12}\right] \times \left[\frac{1}{3}, \frac{7}{12}\right], \quad B = \left[\frac{7}{12}, \frac{5}{6}\right] \times \left[\frac{5}{12}, \frac{2}{3}\right]. \tag{61}$$

The vector field q is plotted in the Figure 11.

Remark 3 *In this test example, the background density is $\rho = 0.6$. It is even more interesting to see what happens when the background density is close to zero. However, our schemes are not performing well in this situation. Indeed, vacuum is a big problem which needs some special treatment. And when the background density is close to zero, the system is almost pressureless, which is also a difficult problem. These problems may be considered in the future work.*

It can be expected that there will be two congested regions forming and moving towards each other with two shocks in the front and two rarefaction waves left behind. These two shocks compress the fluid and cause congestion. This is reflected in Figure 12.

These two shocks with opposite directions meet at a later time. The interaction of these shocks forms a bigger congestion region with higher density, which can be illustrated in Figure 13. The interaction of the two shocks induces the formation of two new shocks moving in the orthogonal direction compared to the initial motion.

The similar result can be obtained by the Gauge 1 method as in Figure 14 and 15.

The difference between the two methods in the two dimensional case is not striking. In order to illustrate them, we look at a cut at $y = 0.5$. The cuts are displayed on Figure 16 and 17.

Similar observations as in the one dimensional case can be made from Figure 16 and 17. The Gauge 1 method provides a little less oscillations in the congestion region but also brings more diffusion.
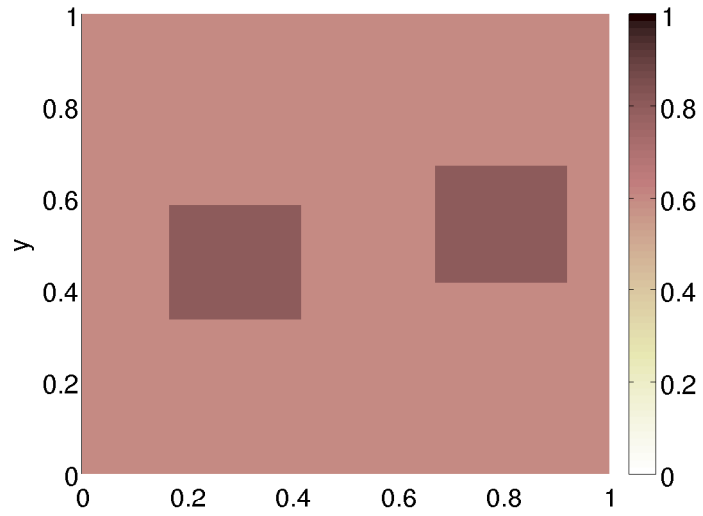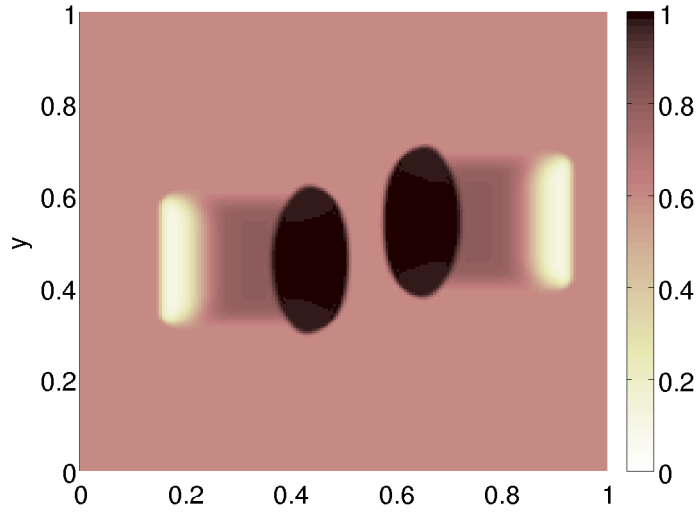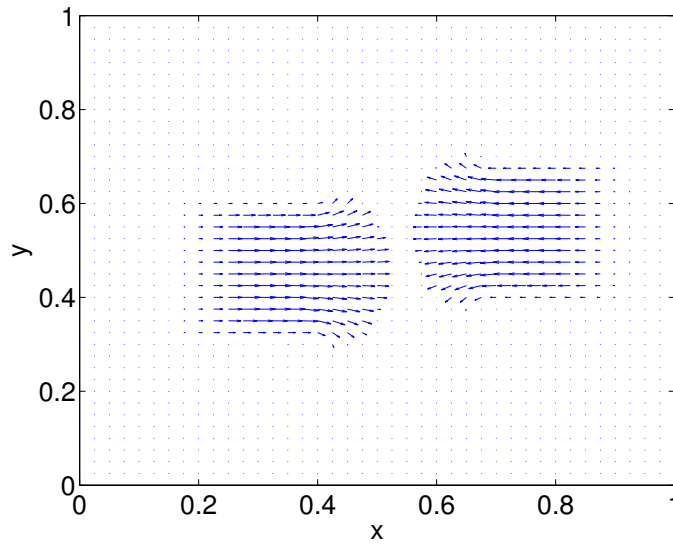
(a) density ρ
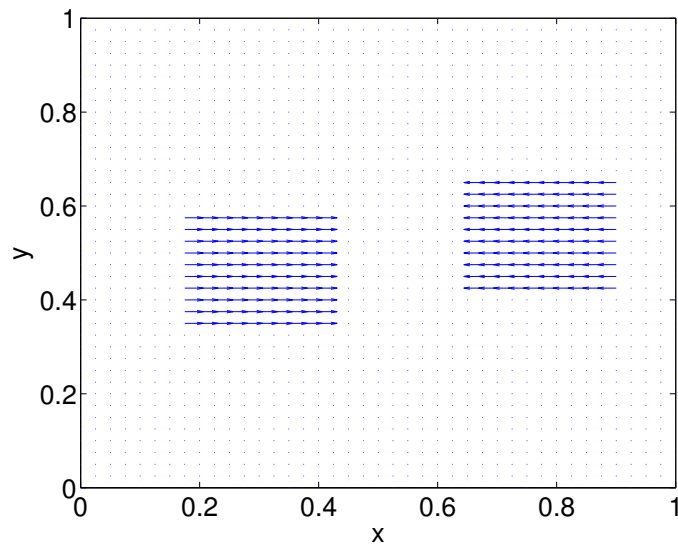
(b) vector field of momentum q

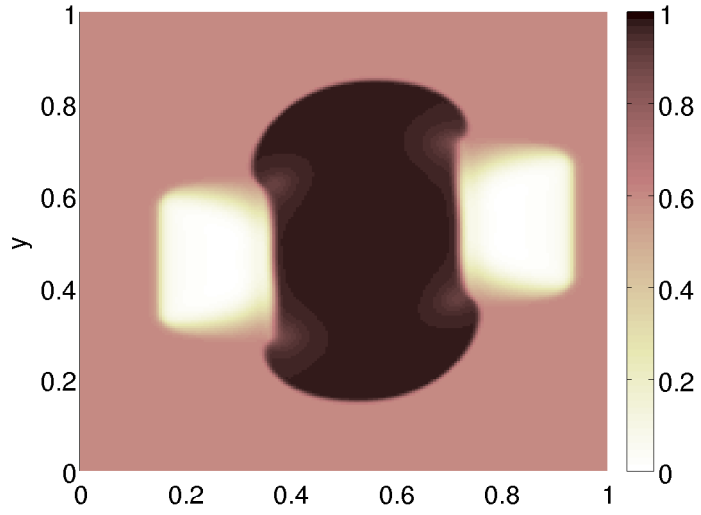Figure 11: The initial data of the density and momentum q, both as functions of x and y.
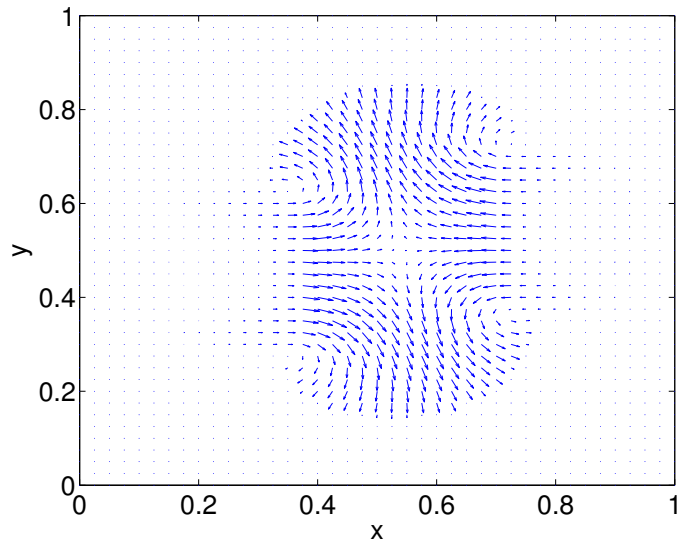
(a) density ρ

(b) vector field of momentum $\boldsymbol{q}$

Figure 12: The Direct method with $\varepsilon = 10^{-4}, \Delta x = 5 \times 10^{-3}, \Delta t = 5 \times 10^{-4}$ at $t = 0.05$. The left graph is for ρ, the right one for vector field q, both as functions of x and y.
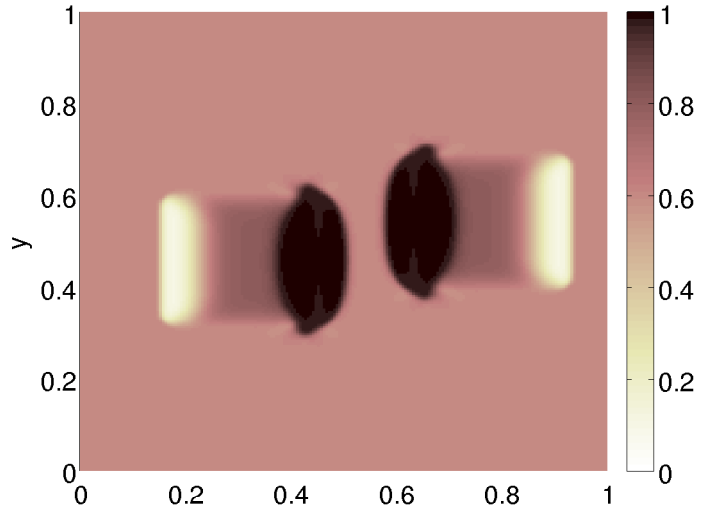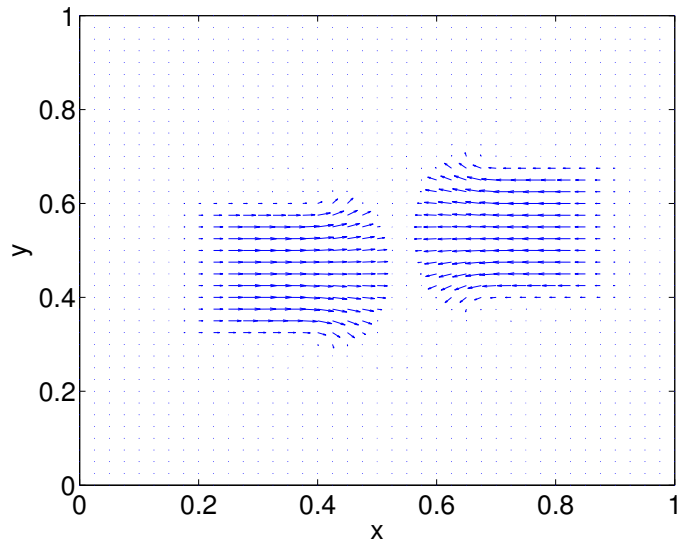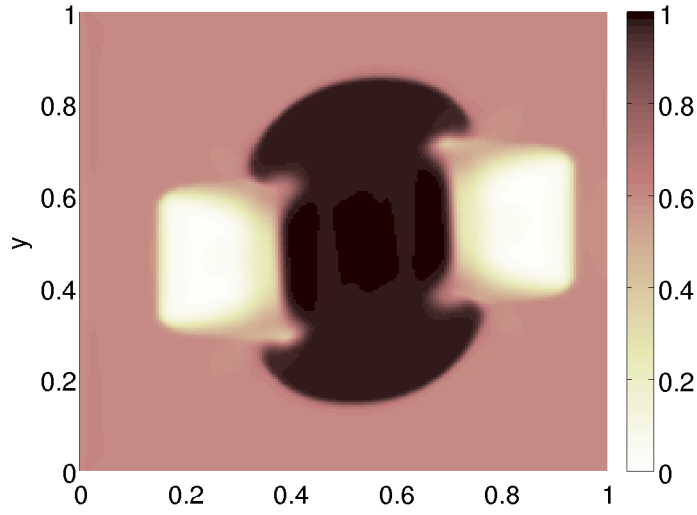
(a) density ρ

(b) vector field of momentum $\boldsymbol{q}$

Figure 13: The Direct method with $\varepsilon = 10^{-4}, \Delta x = 5 \times 10^{-3}, \Delta t = 5 \times 10^{-4}$ at $t = 0.2$. The left graph is for ρ, the right one for vector field q, both as functions of x and y.
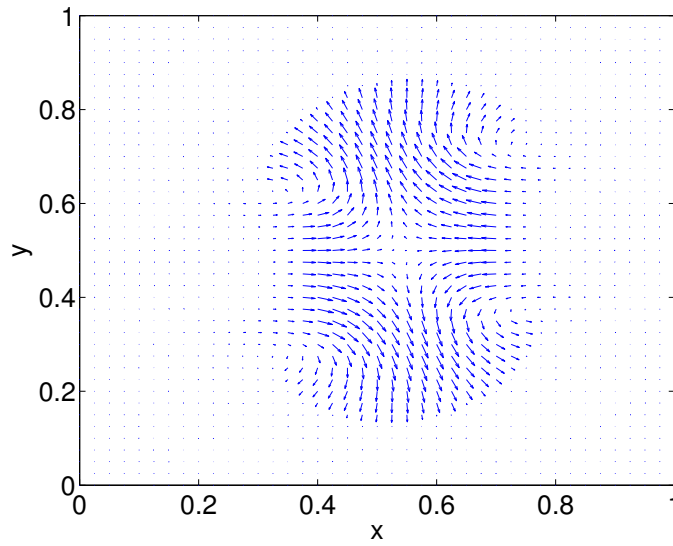
(a) density ρ

(b) vector field of momentum $\boldsymbol{q}$

Figure 14: The Gauge 1 method with $\varepsilon = 10^{-4}, \Delta x = 5 \times 10^{-3}, \Delta t = 5 \times 10^{-4}$ at $t = 0.05$. The left graph is for ρ, the right one for vector field q, both as functions of x and y.
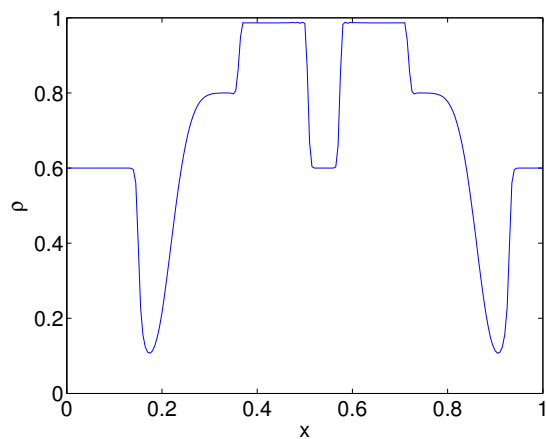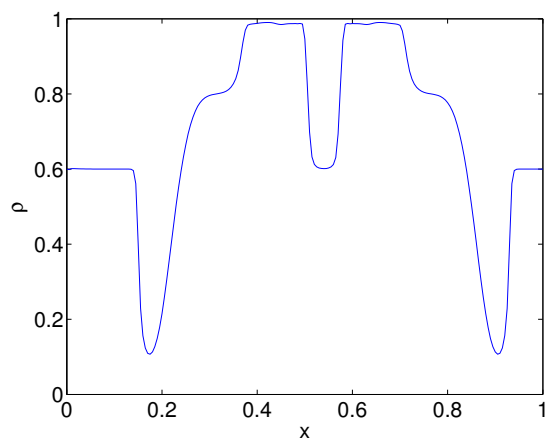
(a) density ρ

(b) vector field of momentum $\boldsymbol{q}$

Figure 15: The Gauge 1 method with $\varepsilon = 10^{-4}, \Delta x = 5 \times 10^{-3}, \Delta t = 5 \times 10^{-4}$ at $t = 0.2$. The left graph is for ρ, the right one for vector field q, both as functions of x and y.
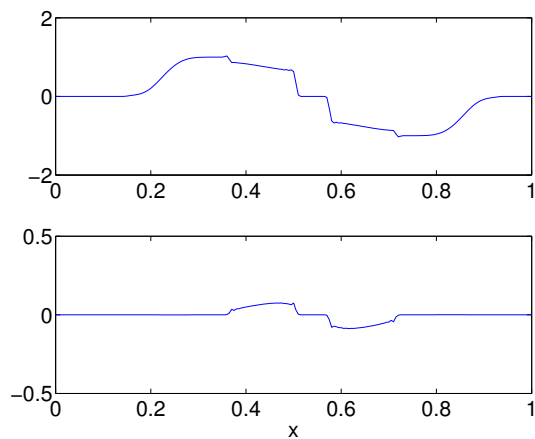
(a) Direct method
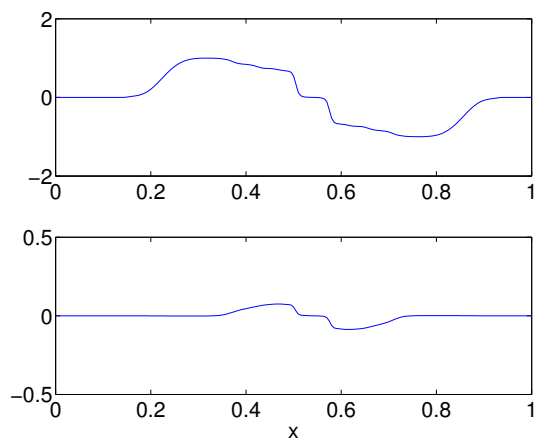

(b) Gauge 1 method

Figure 16: Direct and Gauge 1 methods with $\varepsilon = 10^{-4}, \Delta x = 5 \times 10^{-3}, \Delta t = 5 \times 10^{-4}$ at $t = 0.05$. Cut of the density along the line $y = 0.5$, as a function of x. Left hand: Direct method; right hand: Gauge 1 method.

(a) Direct method

(b) Gauge 1 method

Figure 17: Momentum of the Direct and Gauge 1 methods with $\varepsilon = 10^{-4}, \Delta x = 5 \times 10^{-3}, \Delta t = 5 \times 10^{-4}$ at $t = 0.05$. Cut of the momentum along the line $y = 0.5$, as a function of x. Left hand: Direct method; right hand: Gauge 1 method.

6 Conclusion

In this paper, we have studied the Euler system with a maximal density constraint. A small parameter ε was introduced to measure the stiffness of the constraint. As $\varepsilon \to 0$, the model gives rise to a two-phase model with congested regions (with maximal density) and uncongested regions (with density below the maximal density).

One-dimensional solutions of this asymptotic problem have been investigated to provide the information of the interface conditions. However, it can not characterize the whole dynamics and it is hard to extend to higher dimensional cases. Therefore, we have devised asymptotic preserving numerical schemes, which are valid for all range of ε and thus are capable of capturing the asymptotic dynamics. Two numerical schemes have been considered and compared on both one-dimensional and two dimensional test-cases. They both capture the congested regions well. However, the first method shows some oscillations near the interface between congested and uncongested regions, while the second has much less oscillations but is more diffusive. A careful error analysis in different norms with respect to different parameters (time and space steps, ε) are conducted for a one dimensional test case.

Following [35], the development of second order schemes will be performed in future works. More robust schemes for capturing the divergence free constraint in the congested regions could also be investigated. Coupling our methodology with schemes dedicated to the pressureless gas dynamics could also improve the results in the low density regions. Finally, simulations of the non-conservative model with a supplementary geometric constraint on the speed of the flow [17] will be an interesting problem.

A Appendix : Solutions of the one-dimensional problem: the Riemann problem and the cluster collisions

The one-dimensional version of system (4)-(5) can be written as follows:

$$\partial_t \rho + \partial_x q = 0, \tag{62}$$

$$\partial_t q + \partial_x \left(\frac{q^2}{\rho} \right) + \partial_x (\varepsilon p(\rho)) = 0, \tag{63}$$

where $q(x,t)$ is here a scalar function and x is the position in $\mathbb{R}$. In this section, we first investigate the Riemann problem and the limits of its solutions as $\varepsilon \to 0$

and then we briefly recall the one-dimensional solutions of the limit system (8)-(9)-(10) provided in [12], which consists of the collision of two finite clusters (domain where $\rho = \rho^*$).

A.1   The one-dimensional Riemann problem

The Riemann problem is an initial value problem, where the initial condition is a piece-wise constant function with a discontinuity between two constant states:

$$(\rho_0, q_0)(x) = \begin{cases} (\rho_\ell, q_\ell), & \text{for } x < 0, \\ (\rho_r, q_r), & \text{for } x \geq 0. \end{cases}$$

The solutions of this problem for the Euler system (62)-(63) are well known. So, the strategy is to take the limits of these solutions as ε goes to zero. This provides the solutions of the Riemann problem for the singular asymptotic limit (8)-(9)-(10). Similar studies was carried out in [5] for the isentropic Euler equation, in [9] for a traffic jam model and in [17] for a herding problem.

A.1.1   Shock and rarefaction waves

The material of this section is classical, and is given here only for the reader's convenience.

The two characteristic speeds $\lambda_\pm^\varepsilon$ and the two characteristic fields $\boldsymbol{r}_\pm^\varepsilon$ of the one-dimensional system (62)-(63) are:

$$\lambda_\pm^\varepsilon = u \pm \sqrt{\varepsilon p'(\rho)}, \quad \boldsymbol{r}_\pm^\varepsilon = \begin{pmatrix} 1 \\ u \pm \sqrt{\varepsilon p'(\rho)} \end{pmatrix}.$$

It can be easily checked that both characteristic fields are genuinely non linear for positive densities. Therefore, the solutions of the Riemann problem are made of constant states separated by rarefaction or shock waves [27].

The **rarefaction waves** are continuous self similar solutions: $(\rho(x/t), q(x/t))$. Given a state $(\hat{\rho}, \hat{q})$, the states which can be connected to $(\hat{\rho}, \hat{q})$ by a rarefaction wave are those located on the integral curves $i_\pm^\varepsilon$ of the right eigenvectors of the Jacobian matrix of the flux function issued from $(\hat{\rho}, \hat{q})$. They are given by:

$$\rho'(s) = 1, \quad i_\pm^{\varepsilon\,'}(s) = \hat{u} \pm \sqrt{\varepsilon p'(\rho)}, \quad \rho(0) = \hat{\rho}, \quad i_\pm^\varepsilon(0) = \hat{q},$$

which is equivalent to $i_\pm^{\varepsilon\,'}(\rho) = \hat{u} \pm \sqrt{\varepsilon p'(\rho)}$, $i_\pm^\varepsilon(\hat{\rho}) = \hat{q}$ and then to equation:

$$i_\pm^\varepsilon(\rho) = \rho\hat{u} \pm \rho\sqrt{\varepsilon}(P(\rho) - P(\hat{\rho})), \tag{64}$$

where P is an antiderivative of $\sqrt{p'(u)}/u$ and $\hat{u} = \hat{q}/\hat{\rho}$. The graph of i_-^ε (resp. i_+^ε) is called the 1-integral curve (resp. the 2-integral curve). The following proposition provides several features of the integral curves.

Proposition 1 *(Integral and rarefaction curves)*

1. The 1-integral curve i_-^ε (resp. the 2-integral curve i_+^ε) is concave (resp. convex) as functions of ρ and $i_-^\varepsilon(0) = i_+^\varepsilon(0) = 0$.

2. The limit of the integral curves as ε goes to zero is the union of the straight lines $\{q = \rho\hat{u}\}$ and $\{\rho = \rho^*\}$.

3. Suppose that the state $\hat{\rho}^\varepsilon$ is such that $\hat{\rho}^\varepsilon \to \rho^*$ and $\varepsilon p(\hat{\rho}^\varepsilon) \to \bar{p}$. For all $\rho < \hat{\rho}^\varepsilon$, we have:

$$\left| \frac{i_\pm^\varepsilon(\rho)}{\rho} - \hat{u} \right| \leq \sqrt{\varepsilon} \int_0^{\hat{\rho}^\varepsilon} \frac{\sqrt{p'(u)}}{u} du = \underset{\hat{\rho}^\varepsilon \to \rho^*}{O}(\varepsilon^{\frac{1}{2\gamma}})$$

4. If $(\hat{\rho}, \hat{q})$ is a left state, the right states which can be connected to it by a rarefaction wave are those located on the 1-rarefaction curve $\{(\rho, i_-^\varepsilon(\rho)),\ \rho < \hat{\rho}\}$ or the 2-rarefaction curve $\{(\rho, i_+^\varepsilon(\rho)),\ \rho > \hat{\rho}\}$.

The last point of this proposition stems from the compatibility conditions of the characteristic speeds. The proof of this proposition is classical and omitted.

A **shock wave** is a discontinuity between two constant states, $(\hat{\rho}, \hat{q})$ and (ρ, q), travelling at constant speed σ. The states (ρ, q), which can be connected to $(\hat{\rho}, \hat{q})$ by a shock wave, are determined by the Rankine-Hugoniot conditions:

$$[q] = \sigma[\rho], \quad \left[\frac{q^2}{\rho} + \varepsilon p(\rho)\right] = \sigma[q], \tag{65}$$

where $[f] := f - \hat{f}$ for all quantities f. Easy computations show that the admissible states are of the form $(\rho, h_\pm^\varepsilon(\rho))$, where $h_\pm^\varepsilon$ is :

$$h_\pm^\varepsilon(\rho) = \hat{u} \pm \sqrt{\frac{\rho}{\hat{\rho}}} \sqrt{(\rho - \hat{\rho})(\varepsilon p(\rho) - \varepsilon p(\hat{\rho}))}. \tag{66}$$

and the shock speeds are:

$$\sigma_\pm = \frac{(h_\pm^\varepsilon(\rho) - \hat{q})}{(\rho - \hat{\rho})} = \hat{u} \pm \sqrt{\frac{\rho}{\hat{\rho}}} \sqrt{\frac{(\varepsilon p(\rho) - \varepsilon p(\hat{\rho}))}{(\rho - \hat{\rho})}}. \tag{67}$$

The graph of h_-^ε (resp. h_+^ε) is called the 1-Hugoniot curve (resp. the 2-Hugoniot curve). The following proposition provides several properties of the Hugoniot curves:

Proposition 2 (Hugoniot and shock curves)

1. The 1-Hugoniot function h_-^ε (resp. the 2-Hugoniot function h_+^ε) is concave (resp. convex) and $h_-^\varepsilon(0) = h_+^\varepsilon(0) = 0$.

2. The limits of the graphs of h_-^ε and h_+^ε when ε goes to zero are the union of the straight lines $\{q = \rho\hat{u}\}$ and $\{\rho = \rho^*\}$. This is true also when $\hat{\rho} = \hat{\rho}^\varepsilon$ depends on ε and tends to ρ^*.
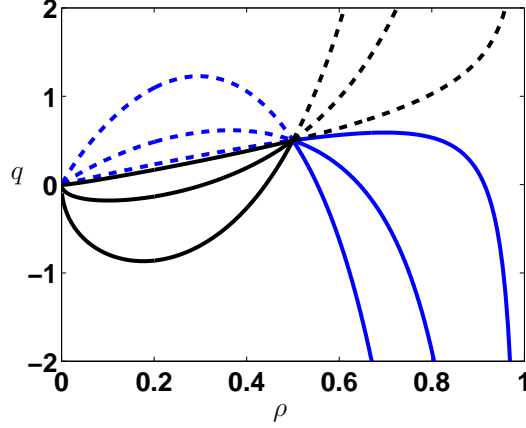
Figure 18: Curves issued from $(\hat{\rho}, \hat{q}) = (0.5, 0.5)$ and $\varepsilon \in \{10, 1, 10^{-2}\}$. In dotted line : the rarefaction curves. In solid line : the shock curves. In blue : the 1-curves. In black : the 2-curves. As $\varepsilon \to 0$, the curves are tending to the straight lines $\{q = \hat{u}\rho\}$ and $\{\rho = \rho^*\}$. Parameters : $k = 2, \rho^* = 1$.

3. If $(\hat{\rho}, \hat{q})$ is a left state, the right states which can be connected to it by an entropic shock wave are those located on the 1-shock curve $\{(\rho, h_-^\varepsilon(\rho)),\ \rho > \hat{\rho}\}$ or the 2-shock curve $\{(\rho, h_+^\varepsilon(\rho)),\ \rho < \hat{\rho}\}$.

The proof of this proposition is classical and omitted.

A.1.2 The Riemann problem for system (62)-(63)

Geometric considerations on the intersection of the integral and Hugoniot curves enable us to solve the Riemann problem [27]. These arguments are really simplified in the limit $\varepsilon \to 0$, due to the much simpler behaviour of the integral and Hugoniot curves: they both converge to union of the straight lines $\{q = \rho\hat{u}\}$ and $\{\rho = \rho^*\}$. This behaviour is illustrated in Fig. 18. The following proposition provides the nature of the solutions of the Riemann problem for ε small enough. It depends on the sign of the relative velocity $u_\ell - u_r$, where $u_\ell = q_\ell/\rho_\ell$ and $u_r = q_r/\rho_r$:

Proposition 3 *Let (ρ_ℓ, q_ℓ), (ρ_r, q_r), left and right states. Then the solutions of the Riemann problem related to (62)-(63) have the following forms:*

1. *If $u_\ell < u_r$, then for ε small enough, the intermediate state is the intersection point of the 1-integral curve issued from $(\rho_\ell, q_\ell, \bar{p}_\ell)$ and the 2-integral curve issued from $(\rho_r, q_r, \bar{p}_r)$. Besides, the intermediate density $\tilde{\rho}$ is lower than ρ_r and ρ_ℓ. This is valid even if ρ_ℓ or/and ρ_r tends to ρ^*.*

40

2. *If $u_\ell > u_r$, then for ε small enough, there are two subcases:*

   - *if $h^\varepsilon_-(\rho^\varepsilon_r) > q_r$ and $h^\varepsilon_+(\rho^\varepsilon_\ell) < q_\ell$, the intermediate state is the intersection point of the 1-Hugoniot curve issued from (ρ_ℓ, q_ℓ) and the 2-Hugoniot curve issued from (ρ_r, q_r).*

   - *if $h^\varepsilon_-(\rho^\varepsilon_r) < q_r$ (resp. $h^\varepsilon_+(\rho^\varepsilon_\ell) > q_\ell$), the intermediate state is the intersection point of the 1-Hugoniot curve (resp. 1-integral curve) issued from (ρ_ℓ, q_ℓ) and the 2-integral curve (resp. 2-Hugoniot curve) issued from (ρ_r, q_r).*

3. *If $u_r = u_\ell$ and $\rho_\ell < \rho_r$ (resp. $\rho_\ell > \rho_r$), then the intermediate state is the intersection point of the 1-Hugoniot curve (resp. 1-integral curve) issued from $(\rho_\ell, q_\ell, \bar{p}_\ell)$ and the 2-integral curve (resp. 2-Hugoniot curve) issued from $(\rho_r, q_r, \bar{p}_r)$. Besides, the intermediate density $\tilde{\rho}$ is the interval $[\rho_\ell, \rho_r]$ (resp. $[\rho_r, \rho_\ell]$). This is valid even if ρ_ℓ or/and ρ_r tends to ρ^*.*

This proposition results from propositions 1 and 2. The proof is omitted here (it is an easy adaptation of the proof of Theorem 1 in [17]). Note that the nature of the curves (integral or Hugoniot curve) implies the nature of the waves involved in the Riemann problem.

A.1.3 The limits of solutions of the Riemann problem.

We introduce the following initial conditions:

$$(\rho^\varepsilon_0, q^\varepsilon_0)(x) = \begin{cases} (\rho^\varepsilon_\ell, q^\varepsilon_\ell), & \text{for } x < 0, \\ (\rho^\varepsilon_r, q^\varepsilon_r), & \text{for } x \geq 0. \end{cases}$$

with $(\rho^\varepsilon_\ell, q^\varepsilon_\ell, \varepsilon p(\rho^\varepsilon_\ell)) \to (\rho_\ell, q_\ell, \bar{p}_\ell)$ and $(\rho^\varepsilon_r, q^\varepsilon_r, \varepsilon p(\rho^\varepsilon_r)) \to (\rho_r, q_r, \bar{p}_r)$ as ε goes to zero.

The following proposition provides the solution when $\rho_\ell, \rho_r < \rho^*$ and so $\bar{p}_\ell = \bar{p}_r = 0$. The nature of the solution only depends on the sign of the relative velocity $u_\ell - u_r$, where $u_\ell = q_\ell/\rho_\ell$ and $u_r = q_r/\rho_r$.

Proposition 4 *(case $\rho_\ell < \rho^*, \rho_r < \rho^*$)*

1. *If $u_\ell - u_r < 0$, then the solution consists of two contact waves connecting the two states to the vacuum. This is summarised in the following diagram:*

$$(\rho_\ell, q_\ell, 0) \quad \overset{contact}{\longrightarrow} \quad (0, q_\ell, 0) \quad \overset{vacuum}{\longrightarrow} \quad (0, q_r, 0) \quad \overset{contact}{\longrightarrow} \quad (\rho_r, q_r, 0).$$

2. *If $u_\ell - u_r > 0$, then the solution consists of two shock waves connecting the left state $(\rho_\ell, q_\ell, 0)$ to an intermediate state $(\rho^*, \tilde{q}, \bar{p})$ and then $(\rho^*, \tilde{q}, \bar{p})$ to the right state $(\rho_r, q_r, 0)$:*

$$(\rho_\ell, q_\ell, 0) \quad \overset{shock}{\longrightarrow} \quad (\rho^*, \tilde{q}, \bar{p}) \quad \overset{shock}{\longrightarrow} \quad (\rho_r, q_r, 0),$$

where the intermediate momentum $\tilde{q}$ and the intermediate pressure $\bar{p}$ are:

$$\tilde{q} = u_\ell \rho^* - \sqrt{\frac{\rho^*}{\rho_\ell}}\sqrt{(\rho^* - \rho_\ell)\bar{p}} = u_r \rho^* + \sqrt{\frac{\rho^*}{\rho_r}}\sqrt{(\rho^* - \rho_r)\bar{p}},$$

$$\bar{p} = (u_\ell - u_r)^2 \left(\sqrt{\frac{\rho^* - \rho_\ell}{\rho_\ell \rho^*}} + \sqrt{\frac{\rho^* - \rho_r}{\rho_r \rho^*}} \right)^{-2},$$

and the shock speeds σ_- and σ_+ are given by:

$$\sigma_- = u_\ell - \sqrt{\frac{\rho^*}{\rho_\ell(\rho^* - \rho_\ell)}}\sqrt{\bar{p}}, \quad \sigma_+ = u_r + \sqrt{\frac{\rho^*}{\rho_r(\rho^* - \rho_r)}}\sqrt{\bar{p}}.$$

3. *If $u_\ell = u_r$, then the solution consists of only one contact wave connecting $(\rho_\ell, q_\ell, 0)$ to $(\rho_r, q_r, 0)$:*

$$(\rho_\ell, q_\ell, 0) \quad \overset{contact}{\longrightarrow} \quad (\rho_r, q_r, 0).$$

It is the same results as those obtained in [12], where they directly proved it by defining a notion of entropy solutions for the asymptotic problem.

In all the following proofs, (ρ_ℓ, q_ℓ), $(\tilde{\rho}, \tilde{q})$, (ρ_r, q_r) will respectively denote the left, the intermediate and the right states involved in each different Riemann problems. λ_-^ε (resp. λ_+^ε) will implicitly refer to the first (resp. second) characteristic speed of the left state (resp. right state). The characteristic speeds related to the intermediate state are denoted: $\tilde{\lambda}_-^\varepsilon$, $\tilde{\lambda}_+^\varepsilon$. In the following, i_-^ε and h_-^ε (resp. i_+^ε and h_+^ε) will refer to the 1-curves (resp. 2-curves) issued from the left state (resp. right state). The notation $[f]_\ell = \tilde{f} - f_\ell$ (resp. $[f]_r = \tilde{f} - f_r$) will denote the difference between the intermediate and the left (resp. the right) values of any quantity f.

Proof 1. From proposition 3, the solution for small ε consists of two rarefaction waves. The intermediate density solves equation $i_-^\varepsilon(\tilde{\rho}) = i_+^\varepsilon(\tilde{\rho})$, that is:

$$\tilde{\rho} u_r \pm \tilde{\rho}\sqrt{\varepsilon}[P(\rho)]_r = \tilde{\rho} u_\ell \pm \tilde{\rho}\sqrt{\varepsilon}[P(\rho)]_\ell$$

Since $\tilde{\rho}$ is lower than ρ_ℓ and ρ_r (and then $[P(\rho)]_r$ and $[P(\rho)]_\ell$ are bounded) and $u_r - u_\ell$ is not zero, it is easy to deduce that the limit solution of this equation is $\tilde{\rho} = 0$, which defines a vacuum state. Besides, λ_-^ε and $\tilde{\lambda}_-^\varepsilon$ tends to u_ℓ (resp. $\tilde{\lambda}_+^\varepsilon$ and λ_+^ε tends to u_r). Therefore, the limit waves are contact waves.

2. From proposition 3, the solution for small ε consists of two shock waves (since $\lim h_+^\varepsilon(\rho_\ell) = \rho_\ell u_r$ and $\lim_-^\varepsilon h_-^\varepsilon(\rho_\ell) = \rho_r q_\ell$). We have $h_{-,\ell}^\varepsilon(\tilde{\rho}) = h_{+,r}^\varepsilon(\tilde{\rho})$, that is:

$$\tilde{\rho} u_\ell - \sqrt{\frac{\tilde{\rho}}{\rho_\ell}}\sqrt{[\rho]_\ell[\varepsilon p(\rho)]_\ell} = \tilde{\rho} u_r + \sqrt{\frac{\tilde{\rho}}{\rho_r}}\sqrt{[\rho]_r[\varepsilon p(\rho)]_r},$$

which yields

$$(u_\ell - u_r) = \sqrt{\frac{[\rho]_\ell[\varepsilon p(\rho)]_\ell}{\rho_\ell \tilde{\rho}}} + \sqrt{\frac{[\rho]_r[\varepsilon p(\rho)]_r}{\rho_r \tilde{\rho}}},$$

Since $u_\ell - u_r$ is different from zero, the limit intermediate pressure, $\lim \varepsilon p(\tilde{\rho}^\varepsilon) = \lim[\varepsilon p(\rho)]_\ell = \lim[\varepsilon p(\rho)]_r$, is not zero. Thus $\tilde{\rho} \to \rho^*$ as $\varepsilon \to 0$. Finally, the limit values of the two shock speeds can be easily inferred from equation (67).

3. Supposing that $\rho_\ell < \rho_r$, then the intermediate density satisfies $\rho_\ell \leq \tilde{\rho}^\varepsilon \leq \rho_r$ and consequently $\lambda^\varepsilon_-, \tilde{\lambda}^\varepsilon_\pm, \lambda^\varepsilon_+ \to u_\ell = u_r$ as ε goes to zero, which yields a unique contact wave.

We now consider the case where the left state is a congested state: $\rho_\ell = \rho^*, \rho_r < \rho^*$ and $\bar{p}_\ell < +\infty$. By a symmetry argument, the case $\rho_\ell < \rho^*, \rho_r = \rho^*$ can be easily deduced. The limits of rarefactions waves when one state tends to congestion lead to the so-called declustering waves:

Definition 1 *(Declustering waves) A declustering wave consists of a shock wave between two congested state, with infinite speed, and with a zero pressure for positive time.*

The following proposition states the solutions of the Riemann problem.

Proposition 5 *(case $\rho_\ell = \rho^*, \rho_r < \rho^*$)*

1. *If $u_\ell - u_r < 0$, then the solution consists of one declustering wave connecting the left state $(\rho^*, q_\ell, \bar{p}_\ell)$ to a congested and pressureless state $(\rho^*, q_\ell, 0)$ and then a contact wave connecting $(\rho^*, q_\ell, 0)$ to vacuum and another contact wave connecting vacuum to the right state $(\rho_r, q_r, 0)$:*

$$(\rho^*, q_\ell, \bar{p}_\ell) \overset{declust.}{\longrightarrow} (\rho^*, q_\ell, 0) \overset{contact}{\longrightarrow} (0, q_\ell, 0) \overset{vacuum}{\longrightarrow} (0, q_r, 0) \overset{contact}{\longrightarrow} (\rho_r, q_r, 0).$$

2. *If $u_\ell - u_r > 0$, then the solution consists of two shock waves connecting the left state $(\rho^*, q_\ell, \bar{p}_\ell)$ to an intermediate congested state $(\rho^*, \tilde{q}, \bar{p})$ and then connecting this intermediate state to the right state speeds $(\rho_r, q_r, 0)$:*

$$(\rho^*, q_\ell, \bar{p}_\ell) \overset{shock}{\longrightarrow} (\rho^*, \tilde{q}, \bar{p}) \overset{shock}{\longrightarrow} (\rho_r, q_r, 0),$$

where the intermediate momentum $\tilde{q}$ and the intermediate pressure $\bar{p}$ are given by:

$$\tilde{q} = \rho^* u_\ell, \quad \bar{p} = \frac{\rho^* \rho_r}{\rho^* - \rho_r}(u_\ell - u_r)^2,$$

and the two speed σ_- and σ_+ are:

$$\sigma_- = -\infty, \quad \sigma_+ = u_r + \sqrt{\frac{\rho^*}{\rho_r}}\sqrt{\frac{\bar{p}}{\rho^* - \rho_r}}.$$

3. *If $u_\ell = u_r$, then the solution consists of one declustering wave connecting the left state $(\rho^*, q_\ell, \bar{p}_\ell)$ to the intermediate state $(\rho^*, q_\ell, 0)$ and one contact wave connecting the intermediate state to the right state $(\rho_r, q_r, 0)$:*

$$(\rho^*, q_\ell, \bar{p}_\ell) \overset{declust.}{\longrightarrow} (\rho^*, q_\ell, 0) \overset{contact}{\longrightarrow} (\rho_r, q_r, 0).$$

43

Proof 1. From proposition 3, the solution for small ε consists of two rarefaction waves and it can be easily checked that the limit intermediate density is zero (thanks to proposition 1, point 3, $\sqrt{\varepsilon}[P(\rho)]_\ell = O(\varepsilon^{\frac{1}{2\gamma}})$). Since ρ_ℓ tends to ρ^*, we have $\lim \lambda_-^\varepsilon = -\infty$ and $\lim \tilde{\lambda}_-^\varepsilon = u_\ell$. The limit of the 2-rarefaction wave is a contact wave (since $\lim \tilde{\lambda}_+^\varepsilon = \lim \lambda_+^\varepsilon = u_r$). Let us look at the limit of the 1-rarefaction wave.

For each possible speed $s \in [\lambda_-^\varepsilon, u_\ell]$ of the rarefaction wave connecting the left state to the intermediate state, we have:

$$s = \lambda_-(\rho(s), q(s)) = \frac{q(s)}{\rho(s)} - \sqrt{\varepsilon p'(\rho(s))}. \tag{68}$$

The state $(\rho(s), q(s))$ belongs to the integral curve and then for $\rho(s) < \rho_\ell$ and according to proposition 1, point 3, $q(s)/\rho(s)$ tends to u_ℓ. If $s \neq u_\ell$, equation (68) implies that $\rho(s)$ has to tend to ρ^* and that $\lim \varepsilon p(\rho(s)) = 0$ since $\lim \varepsilon p'(\rho(s))$ is finite. This yields the definition of a declustering wave, given in definition 1.

2. We have $\lim h_-^\varepsilon(\rho_r) = \rho_r u_\ell > q_r$. According to proposition 3, in order to have a solution which is the limit of two shock waves, we have to prescribe:

$$h_+^\varepsilon(\rho_\ell) = \rho_\ell u_r + \sqrt{\varepsilon}\sqrt{\frac{\rho_\ell}{\rho_r}}\sqrt{[\rho]_r^\ell [p(\rho)]_r^\ell} < q_\ell = \rho_\ell u_\ell,$$

and in the limit:

$$u_r + \sqrt{\frac{(\rho_* - \rho_r)}{\rho_r \rho_*}}\sqrt{\bar{p}_\ell} \leq u_\ell.$$

If $h_+^\varepsilon(\rho_\ell) > q_\ell$, the solution is the limit of a 1-rarefaction wave and a 2-shock wave. According to this discussion, we have to consider two cases but we will see that the limits of the two cases are the same.

The first case corresponds to the limit of two shock waves. The intermediate density is then greater than the left one and so tends to ρ^* too. Besides we have:

$$\tilde{\rho} u_\ell - \sqrt{\frac{\tilde{\rho}}{\rho_\ell}}\sqrt{[\rho]_\ell [\varepsilon p(\rho)]_\ell} = \tilde{\rho} u_r + \sqrt{\frac{\tilde{\rho}}{\rho_r}}\sqrt{[\rho]_r [\varepsilon p(\rho)]_r}, \tag{69}$$

and then by dividing by $\tilde{\rho}$, we get:

$$u_\ell - \sqrt{\frac{[\rho]_\ell [\varepsilon p(\rho)]_\ell}{\tilde{\rho}\rho_\ell}} = u_r + \sqrt{\frac{[\rho]_r [\varepsilon p(\rho)]_r}{\tilde{\rho}\rho_r}} < u_\ell.$$

The last inequality implies that the limit of $\varepsilon p(\tilde{\rho})$ is finite. We denote it by $\bar{p}$. Taking the limit in the equality (69), we obtain

$$u_\ell = u_r + \sqrt{\frac{(\rho^* - \rho_r)}{\rho^* \rho_r}}\sqrt{\bar{p}}.$$

Hence we find the value of $\bar{p}$ as in proposition 5. The propagation speeds are easily deduced from the limit $\varepsilon \to 0$ in (67).

If the solution is the limit of a combination of a rarefaction wave and a shock wave, then the intermediate states satisfies.

$$\tilde{\rho}u_\ell - \tilde{\rho}\sqrt{\varepsilon}[P(\rho)]_\ell = \tilde{\rho}u_r + \sqrt{\frac{\tilde{\rho}}{\rho_r}}\sqrt{[\rho]_r[\varepsilon p(\rho)]_r}.$$

If the intermediate density $\tilde{\rho}^\varepsilon$ did tend to ρ^*, then we would obtain $u_\ell = u_r$ (thanks to proposition 1), which is impossible. Thus the intermediate density tends to ρ^* and the previous expression tends to:

$$\rho^* u_\ell = \rho^* u_r + \sqrt{\frac{\rho^*}{\rho_r}}\sqrt{(\rho^* - \rho_r)\bar{p}},$$

which yields the expected result. Since the pressure is positive, $\tilde{\lambda}^\varepsilon_-$ tends to $-\infty$ which implies that the rarefaction wave turns into a shock wave with infinite propagation speed, i.e. a declustering wave.

3. From proposition 3, the solution is the limit of a combination of a 1-rarefaction wave and a 2-shock wave. Using the fact that $\tilde{\rho}u_\ell = \tilde{\rho}u_r$, the intermediate state $(\tilde{\rho}, \tilde{q})$ satisfies:

$$\tilde{\rho}\varepsilon[P(\rho)]_\ell = \sqrt{\frac{\rho}{\rho_\ell}}\sqrt{[\rho]_r[\varepsilon p(\rho)]_r}.$$

So $[\rho]_r[\varepsilon p(\rho)]_r \to 0$ (since $\varepsilon P(\tilde{\rho}) < \varepsilon P(\rho_\ell)$ tends to zero) and either $\tilde{\rho}$ tends to ρ_r or $\varepsilon p(\tilde{\rho})$ tends to zero. Actually, whatever the limit value of the intermediate density, the intermediate state disappears. Indeed, let us consider all the possible cases.

Either $\tilde{\rho} \to \rho_r$. Then the 2-shock wave disappears and the 1-rarefaction wave tends to the sum of a declustering wave and a contact wave, which can be proven as in the case 1 of this proof.

Or $\lim \tilde{\rho} \in]\rho_r, \rho^*[$. It is easy to check that the 2-shock wave becomes a contact wave and the intermediate state disappears since $\tilde{\lambda}^\varepsilon_+, \tilde{\lambda}^\varepsilon_- \to u_\ell$. Like in the case 1 of this proof, the 1-rarefaction wave leads to declustering wave and a contact wave, which superimposes on the one coming from the 2-shock wave.

Or $\lim \tilde{\rho} = \rho^*$. Then we know that $\varepsilon p(\tilde{\rho})$ tends to zero. Thus the 1-rarefaction wave tends to a declustering wave and the 2-shock wave tends to a contact wave.

In all the cases, the limit solution is the one given in proposition 5.

Finally, we consider the case where both the left and right asymptotic states are congested: $\rho_\ell = \rho_r = \rho^*$. Besides, we assume that $\bar{p}_\ell$ and $\bar{p}_r$ are finite.

Proposition 6 (case $\rho_\ell = \rho^*, \rho_r = \rho^*, \rho^\varepsilon_\ell > \rho^\varepsilon_r$)

1. If $u_\ell - u_r < 0$, then the solution consists of one declustering wave connecting the left state $(\rho^*, q_\ell, \bar{p}_\ell)$ to a congested and pressureless state $(\rho^*, q_\ell, 0)$,

then two contact waves connecting $(\rho^*, q_\ell, 0)$ to vacuum and then vacuum to $(\rho^*, q_r, 0)$ and another declustering wave connecting $(\rho^*, q_r, 0)$ to the right state $(\rho_r, q_r, 0)$:

$$(\rho^*, q_\ell, \bar{p}_\ell) \overset{declust.}{\longrightarrow} (\rho^*, q_\ell, 0) \overset{contact}{\longrightarrow} (0, q_\ell, 0) \overset{vacuum}{\longrightarrow} (0, q_r, 0) \overset{contact}{\longrightarrow} (\rho^*, q_r, 0) \overset{declust.}{\longrightarrow} (\rho^*, q_r, \bar{p}_r).$$

2. *If $u_\ell - u_r > 0$, then the solution consists of two shock waves with infinite propagation speed connecting the left state $(\rho^*, q_\ell, \bar{p}_\ell)$ to an intermediate congested state $(\rho^*, \tilde{q}, +\infty)$ with infinite pressure and then this intermediate state to the right state $(\rho^*, q_r, \bar{p}_r)$:*

$$(\rho^*, q_\ell, \bar{p}_\ell) \quad \overset{shock}{\longrightarrow} \quad (\rho^*, \tilde{q}, +\infty) \quad \overset{shock}{\longrightarrow} \quad (\rho^*, q_r, \bar{p}_r),$$

where $\tilde{q}$ is the unique solution of:

$$\frac{[q]_\ell}{[q]_r} = \left(\frac{\bar{p}_r}{\bar{p}_\ell} \right)^{\frac{1}{2\gamma}}.$$

3. *If $u_\ell = u_r$, then the solution consists of a uniform constant state $(\rho^*, q_r, \bar{p}_r)$.*

Proof 1. The arguments are similar to those used in the proof of the first case of the previous proposition.

2. From proposition 3, the solution is the limit of two shock waves if for small ε, we have the following inequalities:

$$h_+^\varepsilon(\rho_\ell^\varepsilon) = \rho_\ell^\varepsilon u_r + \sqrt{\varepsilon} \sqrt{\frac{\rho_\ell^\varepsilon}{\rho_r^\varepsilon}} \sqrt{[\rho]_r^\ell [p(\rho)]_r^\ell} < q_\ell = \rho_\ell^\varepsilon u_\ell,$$

$$h_-^\varepsilon(\rho_r^\varepsilon) = \rho_r^\varepsilon u_\ell + \sqrt{\varepsilon} \sqrt{\frac{\rho_r^\varepsilon}{\rho_\ell^\varepsilon}} \sqrt{[\rho]_r^\ell [p(\rho)]_r^\ell} > q_r = \rho_r^\varepsilon u_r.$$

Here, these inequalities are always satisfied : their limit is $u_r < u_\ell$ since $\varepsilon[p(\rho)]_r^\ell$ is bounded and $[\rho]_r^\ell \to 0$. The intermediate density $\tilde{\rho}$ satisfies:

$$u_\ell - \sqrt{\frac{[\rho]_\ell [\varepsilon p(\rho)]_\ell}{\tilde{\rho} \rho_\ell}} = u_r + \sqrt{\frac{[\rho]_r [\varepsilon p(\rho)]_r}{\tilde{\rho} \rho_r}}.$$

Therefore, $\varepsilon p(\tilde{\rho})$ cannot be bounded (which would imply $u_\ell = u_r$ since $[\rho]_\ell$ and $[\rho]_r$ tends to zero). So $\varepsilon p(\tilde{\rho})$ tends to $+\infty$ as $\varepsilon \to 0$. From the Rankine-Hugoniot relations, we have

$$[\rho q + \varepsilon p(\rho)]_\ell [\rho]_\ell = [q]_\ell^2,$$
$$[\rho q + \varepsilon p(\rho)]_r [\rho]_r = [q]_r^2$$

Taking the limit of their quotient, we obtain:

$$\lim \frac{[\varepsilon p(\rho)]_\ell [\rho]_\ell}{[\varepsilon p(\rho)]_r [\rho]_r} = \left(\frac{[q]_\ell}{[q]_r} \right)^2, \tag{70}$$

Besides, we have:

$$\frac{[\varepsilon p(\rho)]_\ell [\rho]_\ell}{[\varepsilon p(\rho)]_r [\rho]_r} \underset{\varepsilon \to 0}{\sim} \frac{[\rho]_\ell}{[\rho]_r} \underset{\varepsilon \to 0}{\sim} \frac{\rho^* - \rho_\ell}{\rho^* - \rho_r}$$

where the last equivalence results from the fact that $(\rho^* - \tilde{\rho}) = o(\varepsilon^{\frac{1}{\gamma}})$ and $(\rho^* - \rho_{\ell,r}) = O(\varepsilon^{\frac{1}{\gamma}})$. Finally, we have:

$$\frac{\rho^* - \rho_\ell}{\rho^* - \rho_r} = \left(\frac{\varepsilon p(\rho_r)}{\varepsilon p(\rho_\ell)}\right)^{\frac{1}{\gamma}} \underset{\varepsilon \to 0}{\to} \left(\frac{\bar{p}_r}{\bar{p}_\ell}\right)^{\frac{1}{\gamma}}$$

This last result, combined with eq. (70), provides an equation for the intermediate momentum.

3. Let us suppose that $\rho_\ell^\varepsilon > \rho_r^\varepsilon$. The intermediate density satisfies $\rho_r^\varepsilon < \tilde{\rho}^\varepsilon < \rho_\ell^\varepsilon$ and so tends to ρ^*. The intermediate momentum $\tilde{q}$ tends to $\rho^* u_\ell$. The 1-rarefaction wave tends to a shock wave with infinite propagation speed (since $\tilde{\lambda}_-^\varepsilon$ and λ_-^ε tend to $-\infty$), i.e. a declustering wave. We have now to determine $\bar{p}$. We have

$$\sqrt{\frac{\tilde{\rho}}{\rho_r}} \sqrt{[\rho]_r [\varepsilon p(\rho)]_r} = -\sqrt{\varepsilon}[P(\rho)]_\ell.$$

Since $\tilde{\rho} - \rho_\ell \to 0$, we have $-[P(\rho)]_\ell \sim (\rho_\ell - \tilde{\rho})P'(\rho_\ell)$. We have $P'(\rho_\ell) \sim C(\rho^* - \rho_\ell)^{-\frac{\gamma+1}{2}}$. Then we have $P'(\rho_\ell) \sim C(\varepsilon^{\frac{1}{\gamma}})^{-\frac{\gamma+1}{2}} = C\varepsilon^{-\frac{1}{2}-\frac{1}{2\gamma}}$ (since $(\rho_* - \rho_\ell) = O(\varepsilon^{\frac{1}{\gamma}})$). Besides $(\rho_\ell - \tilde{\rho}) \leq (\rho_* - \rho_r) = O(\varepsilon^{\frac{1}{\gamma}})$ and $[\rho]_r = O(\varepsilon^{\frac{1}{\gamma}})$ and , so we have

$$[\varepsilon p(\rho)]_r = \frac{\rho_r}{\tilde{\rho}} \frac{(-\sqrt{\varepsilon}[P(\rho)]_\ell)^2}{[\rho]_r} = O(\varepsilon^{\frac{1}{\gamma}}).$$

So $\varepsilon p(\tilde{\rho})$ tends to $\bar{p}_r$. The 2-shock wave disappears (since the intermediate and the right state are identical). Then the limit solution consists of an instantaneous propagation of the right state.

A.2   The one-dimensional cluster collisions

The Riemann problem where both the left and right states are congested is ill-posed since infinite pressure may appear to correct the discontinuity in the pressure in the incompressible domain. Like in [17, 12, 8], we have to restrict to the collision of finite congested domains. Consider two one dimensional clusters which collides at a time t_c. Before collision, the left (resp. right) cluster at time $t < t_c$ extends between $a_\ell(t)$ and $b_\ell(t)$ (resp. $a_r(t)$ and $b_r(t)$) and moves with speed:

$$u_\ell = a'_\ell(t) = b'_\ell(t) \quad (\text{resp. } u_r = a'_r(t) = b'_r(t)).$$

After collision, the two clusters aggregate and form a new cluster at time $t > t_c$ extending between $a(t)$ and $b(t)$ and moving with speed $u = a'(t) = b'(t)$. Therefore, ρ and u are given for $t < t_c$ by:

$$\rho = \rho^* 1_{[a_\ell(t), b_\ell(t)]} + \rho^* 1_{[a_r(t), b_r(t)]}, \quad u = u_\ell 1_{[a_\ell(t), b_\ell(t)]} + u_r 1_{[a_r(t), b_r(t)]},$$

and for $t > t_c$ by:
$$\rho = \rho^* 1_{[a(t),b(t)]}, \quad u = u 1_{[a(t),b(t)]}.$$

where 1_I denotes the indicator function of interval I. We denote by $m = b_\ell(t_c) = a_r(t_c)$ the collision point. We look for a pressure written as $\bar{p}(x,t) = \pi(x)\delta(t - t_c)$. Conditions to have such kind of solution for the one-dimensional version of (8)-(9)-(10) was obtained in [12]. We report them in the following proposition.

Proposition 7 *1- Supposing that $\bar{p}(x,t) = \pi(x)\delta(t - t_c)$ where π is continuous and zero outside the clusters, then u and π have to satisfy*

$$(u - u_\ell)(m - a(t_c)) + (u - u_r)(b(t_c) - m) = 0,$$

$$\tag{71}$$

$$\pi(x) = \begin{cases} \rho^*(u - u_\ell)(m - x) \\ \quad + \rho^*(u - u_r)(b(t_c) - m), & \text{if } x \in [a(t_c), m], \\ \rho^*(u - u_r)(b(t_c) - x), & \text{if } x \in [m, b(t_c)], \end{cases} \tag{72}$$

2 - Under conditions (71)-(72), $(\rho, \rho u, \bar{p})$ is a solution (in a distributional sense) to the one-dimensional version of system (8)-(9)-(10).

Remark : We note that the solutions where the two clusters aggregate after the collision is one among possibly multiple solutions. Another solution is given by a bounce of the two clusters one against each other leading to a reflection of the velocities. There are infinitely many such reflections which preserve total momentum.

B   Appendix : The two dimensional full time and space discretization

The Direct method: We consider the 2D case with domain $\Omega = [0,1] \times [0,1]$. Denote $(x_i, y_j) = (i\Delta x, j\Delta y)$, $i = 0, \cdots, M_1; j = 0, \cdots, M_2$, where $M_1 = 1/\Delta x$, $M_2 = 1/\Delta y$. Let $U = (\rho, \boldsymbol{q})^T, \boldsymbol{q} = (q_1, q_2)^T$ and $U_{i,j} = U(x_j, y_j)$. To simplify the notation, we define

$$\boldsymbol{F}(U) = \begin{pmatrix} \frac{q_1^2}{\rho} + \varepsilon p_0(\rho) \\ \frac{q_1 q_2}{\rho} \end{pmatrix}, \boldsymbol{G}(U) = \begin{pmatrix} \frac{q_1 q_2}{\rho} \\ \frac{q_2^2}{\rho} + \varepsilon p_0(\rho) \end{pmatrix}.$$

Then (1) and (2) can be written as

$$\partial_t \rho + \partial_x q_1 + \partial_y q_2 = 0,$$
$$\partial_t \boldsymbol{q} + \partial_x \boldsymbol{F}(U) + \partial_y \boldsymbol{G}(U) + \nabla_{\boldsymbol{x}}(\varepsilon p_1(\rho)) = 0.$$

Denote

$$\boldsymbol{F}^n = \begin{pmatrix} \frac{(q_1^n)^2}{\rho^n} + \varepsilon p_0(\rho^n) \\ \frac{q_1^n q_2^n}{\rho^n} \end{pmatrix}, \quad \boldsymbol{G}^n = \begin{pmatrix} \frac{q_1^n q_2^n}{\rho^n} \\ \frac{(q_2^n)^2}{\rho^n} + \varepsilon p_0(\rho^n) \end{pmatrix},$$

$$\nabla_{i,j}(\varepsilon p_1)^{n+1} = \begin{pmatrix} D_{i,j}^x(\varepsilon p_1(\rho))^{n+1} \\ D_{i,j}^y(\varepsilon p_1(\rho))^{n+1} \end{pmatrix} = \begin{pmatrix} D_{i,j}^x(\varepsilon p_1(\rho^{n+1})) \\ D_{i,j}^y(\varepsilon p_1(\rho^{n+1})) \end{pmatrix},$$

where $D_{i,j}^x u, D_{i,j}^y u$ are the centered difference operators for any scalar functions u defined as follows

$$D_{i,j}^x u = \frac{u_{i+1,j} - u_{i-1,j}}{2\Delta x}, \quad D_{i,j}^y u = \frac{u_{i,j+1} - u_{i,j-1}}{2\Delta y}.$$

We also define the eigenvalues of the Jacobian matrix for two one-dimensional hyperbolic system as follows:

$$\lambda^{(1)} = \frac{q_1}{\rho}, \frac{q_1}{\rho} \pm \sqrt{\varepsilon p_0'(\rho)}, \quad \lambda^{(2)} = \frac{q_2}{\rho}, \frac{q_2}{\rho} \pm \sqrt{\varepsilon p_0'(\rho)}.$$

With the above notations, the full discretization of the scheme takes the following form:

$$\frac{\rho_{i,j}^{n+1} - \rho_{i,j}^n}{\Delta t} + \frac{1}{\Delta x}\left(Q_{i+\frac{1}{2},j}^{n+\frac{1}{2}} - Q_{i-\frac{1}{2},j}^{n+\frac{1}{2}}\right) + \frac{1}{\Delta y}\left(\tilde{Q}_{i,j+\frac{1}{2}}^{n+\frac{1}{2}} - \tilde{Q}_{i,j-\frac{1}{2}}^{n+\frac{1}{2}}\right) = 0,$$

$$\frac{q_{i,j}^{n+1} - q_{i,j}^n}{\Delta t} + \frac{1}{\Delta x}\left(F_{i+\frac{1}{2},j}^n - F_{i-\frac{1}{2},j}^n\right) + \frac{1}{\Delta y}\left(G_{i,j+\frac{1}{2}}^n - G_{i,j-\frac{1}{2}}^n\right) + \nabla_{i,j}(\varepsilon p_1)^{n+1} = 0,$$

where the fluxes are

$$Q_{i+\frac{1}{2},j}^{n+\frac{1}{2}} = \frac{1}{2}\left\{(q_1)_{i+1,j}^{n+1} + (q_1)_{i,j}^{n+1}\right\} - \frac{1}{2}C_{i+\frac{1}{2},j}(\rho_{i+1,j}^n - \rho_{i,j}^n),$$

$$\tilde{Q}_{i,j+\frac{1}{2}}^{n+\frac{1}{2}} = \frac{1}{2}\left\{(q_2)_{i,j+1}^{n+1} + (q_2)_{i,j}^{n+1}\right\} - \frac{1}{2}C_{i,j+\frac{1}{2}}(\rho_{i,j+1}^n - \rho_{i,j}^n),$$

$$F_{i+\frac{1}{2},j}^n = \frac{1}{2}\left\{F_{i+1,j}^n + F_{i,j}^n\right\} - \frac{1}{2}C_{i+\frac{1}{2},j}(q_{i+1,j}^n - q_{i,j}^n),$$

$$G_{i,j+\frac{1}{2}}^n = \frac{1}{2}\left\{G_{i,j+1}^n + G_{i,j}^n\right\} - \frac{1}{2}C_{i,j+\frac{1}{2}}(q_{i,j+1}^n - q_{i,j}^n).$$

and

$$C_{i+\frac{1}{2},j} = \max\{|\lambda_{i,j}^{(1)}|, |\lambda_{i+1,j}^{(1)}|, |\lambda_{i,j}^{(2)}|, |\lambda_{i+1,j}^{(2)}|\},$$

$$C_{i,j+\frac{1}{2}} = \max\{|\lambda_{i,j}^{(1)}|, |\lambda_{i,j+1}^{(1)}|, |\lambda_{i,j}^{(2)}|, |\lambda_{i,j+1}^{(2)}|\}.$$

Similar to the one-dimensional case, by inserting the momentum equation

into the density equation, we can get the following elliptic equation

$$\rho_{i,j}^{n+1} - \frac{\Delta t^2}{4} \Bigg\{ \frac{1}{\Delta x^2} \left[\varepsilon p_1(\rho_{i+2,j}^{n+1}) - 2\varepsilon p_1(\rho_{i,j}^{n+1}) + \varepsilon p_1(\rho_{i-2,j}^{n+1}) \right]$$

$$+ \frac{1}{\Delta y^2} \left[\varepsilon p_1(\rho_{i,j+2}^{n+1}) - 2\varepsilon p_1(\rho_{i,j}^{n+1}) + \varepsilon p_1(\rho_{i,j-2}^{n+1}) \right] \Bigg\}$$

$$= \rho_{i,j}^n - \Delta t (D_{i,j}^x q_1^n + D_{i,j}^y q_2^n)$$

$$+ \frac{\Delta t^2}{2} \Bigg\{ \frac{1}{\Delta x^2} \left[(\boldsymbol{F}_{i+3/2,j}^n)^{(1)} - (\boldsymbol{F}_{i+1/2,j}^n)^{(1)} - (\boldsymbol{F}_{i-1/2,j}^n)^{(1)} + (\boldsymbol{F}_{i-3/2,j}^n)^{(1)} \right]$$

$$+ \frac{1}{\Delta x \Delta y} \left[(\boldsymbol{G}_{i+1,j+1/2}^n)^{(1)} - (\boldsymbol{G}_{i+1,j-1/2}^n)^{(1)} - (\boldsymbol{G}_{i-1,j+1/2}^n)^{(1)} + (\boldsymbol{G}_{i-1,j-1/2}^n)^{(1)} \right]$$

$$+ \frac{1}{\Delta x \Delta y} \left[(\boldsymbol{F}_{i+1/2,j+1}^n)^{(2)} - (\boldsymbol{F}_{i-1/2,j+1}^n)^{(2)} - (\boldsymbol{F}_{i+1/2,j-1}^n)^{(2)} + (\boldsymbol{F}_{i-1/2,j-1}^n)^{(2)} \right]$$

$$+ \frac{1}{\Delta y^2} \left[(\boldsymbol{G}_{i,j+3/2}^n)^{(2)} - (\boldsymbol{G}_{i,j+1/2}^n)^{(2)} - (\boldsymbol{G}_{i,j-1/2}^n)^{(2)} + (\boldsymbol{G}_{i,j-3/2}^n)^{(2)} \right] \Bigg\}$$

$$+ \frac{\Delta t}{2\Delta x} \left[C_{i+\frac{1}{2},j}(\rho_{i+1,j}^n - \rho_{i,j}^n) - C_{i-\frac{1}{2},j}(\rho_{i,j}^n - \rho_{i-1,j}^n) \right]$$

$$+ \frac{\Delta t}{2\Delta y} \left[C_{i,j+\frac{1}{2}}(\rho_{i,j+1}^n - \rho_{i,j}^n) - C_{i,j-\frac{1}{2}}(\rho_{i,j}^n - \rho_{i,j-1}^n) \right].$$

$$(73)$$

Here $(\boldsymbol{F}_{i+1/2,j}^n)^{(1)}$ is the first component of the vector $\boldsymbol{F}_{i+1/2,j}^n$. Also similar to the one-dimensional case, we solve the above elliptic equation to get first p_1^{n+1} then ρ^{n+1}. And once ρ^{n+1} is derived, we can get q^{n+1} explicitly.

$$\boldsymbol{q}_{i,j}^{n+1} = \boldsymbol{q}_{i,j}^n - \frac{\Delta t}{\Delta x} \left(\boldsymbol{F}_{i+\frac{1}{2},j}^n - \boldsymbol{F}_{i-\frac{1}{2},j}^n \right) - \frac{\Delta t}{\Delta y} \left(\boldsymbol{G}_{i,j+\frac{1}{2}}^n - \boldsymbol{G}_{i,j-\frac{1}{2}}^n \right) - \Delta t \nabla_{i,j}(\varepsilon p_1)^{n+1}.$$

Gauge method: The Gauge method can be implemented in a similar way as the 1D case. Indeed, we have the same elliptic equation for p_1 (73) and the following equations:

$$\frac{1}{4\Delta x^2} \left[\varphi_{i+2,j}^{n+1} - 2\varphi_{i,j}^{n+1} + \varphi_{i-2,j}^{n+1} \right] + \frac{1}{4\Delta y^2} \left[\varphi_{i,j+2}^{n+1} - 2\varphi_{i,j}^{n+1} + \varphi_{i,j-2}^{n+1} \right]$$

$$= \frac{\rho_{i,j}^{n+1} - \rho_{i,j}^n}{\Delta t} - \frac{1}{2\Delta x} \left[C_{i+\frac{1}{2},j}(\rho_{i+1,j}^n - \rho_{i,j}^n) - C_{i-\frac{1}{2},j}(\rho_{i,j}^n - \rho_{i-1,j}^n) \right]$$

$$- \frac{1}{2\Delta y} \left[C_{i,j+\frac{1}{2}}(\rho_{i,j+1}^n - \rho_{i,j}^n) - C_{i,j-\frac{1}{2}}(\rho_{i,j}^n - \rho_{i,j-1}^n) \right],$$

$$\frac{1}{4\Delta x^2} \left[P_{i+2,j}^{n+1} - 2P_{i,j}^{n+1} + P_{i-2,j}^{n+1} \right] + \frac{1}{4\Delta y^2} \left[P_{i,j+2}^{n+1} - 2P_{i,j}^{n+1} + P_{i,j-2}^{n+1} \right]$$

$$= -\frac{1}{2} \Bigg\{ \frac{1}{\Delta x^2} \left[(\boldsymbol{F}_{i+3/2,j}^n)^{(1)} - (\boldsymbol{F}_{i+1/2,j}^n)^{(1)} - (\boldsymbol{F}_{i-1/2,j}^n)^{(1)} + (\boldsymbol{F}_{i-3/2,j}^n)^{(1)} \right]$$

$$+ \frac{1}{\Delta x \Delta y} \left[(\boldsymbol{G}_{i+1,j+1/2}^n)^{(1)} - (\boldsymbol{G}_{i+1,j-1/2}^n)^{(1)} - (\boldsymbol{G}_{i-1,j+1/2}^n)^{(1)} + (\boldsymbol{G}_{i-1,j-1/2}^n)^{(1)} \right]$$

$$+ \frac{1}{\Delta x \Delta y} \left[(\boldsymbol{F}_{i+1/2,j+1}^n)^{(2)} - (\boldsymbol{F}_{i-1/2,j+1}^n)^{(2)} - (\boldsymbol{F}_{i+1/2,j-1}^n)^{(2)} + (\boldsymbol{F}_{i-1/2,j-1}^n)^{(2)} \right]$$

$$+ \frac{1}{\Delta y^2} \left[(\boldsymbol{G}_{i,j+3/2}^n)^{(2)} - (\boldsymbol{G}_{i,j+1/2}^n)^{(2)} - (\boldsymbol{G}_{i,j-1/2}^n)^{(2)} + (\boldsymbol{G}_{i,j-3/2}^n)^{(2)} \right] \bigg\},$$

$$\frac{\boldsymbol{a}_{i,j}^{n+1} - \boldsymbol{a}_{i,j}^n}{\Delta t} + \frac{1}{\Delta x} \left(\boldsymbol{F}_{i+\frac{1}{2},j}^n - \boldsymbol{F}_{i-\frac{1}{2},j}^n \right) + \frac{1}{\Delta y} \left(\boldsymbol{G}_{i,j+\frac{1}{2}}^n - \boldsymbol{G}_{i,j-\frac{1}{2}}^n \right) + \nabla_{i,j} P^{n+1} = 0,$$

$$\boldsymbol{q}_{i,j}^{n+1} = \boldsymbol{a}_{i,j}^{n+1} - \nabla_{i,j} \varphi^{n+1}.$$

This is the Gauge 2 method. And similar to the one dimensional case, we will mainly test the Gauge 1 method with a smaller stencil in the Laplace equation of φ and P:

$$\frac{1}{\Delta x^2} \left[\varphi_{i+1,j}^{n+1} - 2\varphi_{i,j}^{n+1} + \varphi_{i-1,j}^{n+1} \right] + \frac{1}{\Delta y^2} \left[\varphi_{i,j+1}^{n+1} - 2\varphi_{i,j}^{n+1} + \varphi_{i,j-1}^{n+1} \right]$$

$$= \frac{\rho_{i,j}^{n+1} - \rho_{i,j}^n}{\Delta t} - \frac{1}{2\Delta x} \left[C_{i+\frac{1}{2},j}(\rho_{i+1,j}^n - \rho_{i,j}^n) - C_{i-\frac{1}{2},j}(\rho_{i,j}^n - \rho_{i-1,j}^n) \right]$$

$$- \frac{1}{2\Delta y} \left[C_{i,j+\frac{1}{2}}(\rho_{i,j+1}^n - \rho_{i,j}^n) - C_{i,j-\frac{1}{2}}(\rho_{i,j}^n - \rho_{i,j-1}^n) \right],$$

$$\frac{1}{\Delta x^2} \left[P_{i+1,j}^{n+1} - 2P_{i,j}^{n+1} + P_{i-1,j}^{n+1} \right] + \frac{1}{\Delta y^2} \left[P_{i,j+1}^{n+1} - 2P_{i,j}^{n+1} + P_{i,j-1}^{n+1} \right]$$

$$= -\frac{1}{2} \bigg\{ \frac{1}{\Delta x^2} \left[(\boldsymbol{F}_{i+3/2,j}^n)^{(1)} - (\boldsymbol{F}_{i+1/2,j}^n)^{(1)} - (\boldsymbol{F}_{i-1/2,j}^n)^{(1)} + (\boldsymbol{F}_{i-3/2,j}^n)^{(1)} \right]$$

$$+ \frac{1}{\Delta x \Delta y} \left[(\boldsymbol{G}_{i+1,j+1/2}^n)^{(1)} - (\boldsymbol{G}_{i+1,j-1/2}^n)^{(1)} - (\boldsymbol{G}_{i-1,j+1/2}^n)^{(1)} + (\boldsymbol{G}_{i-1,j-1/2}^n)^{(1)} \right]$$

$$+ \frac{1}{\Delta x \Delta y} \left[(\boldsymbol{F}_{i+1/2,j+1}^n)^{(2)} - (\boldsymbol{F}_{i-1/2,j+1}^n)^{(2)} - (\boldsymbol{F}_{i+1/2,j-1}^n)^{(2)} + (\boldsymbol{F}_{i-1/2,j-1}^n)^{(2)} \right]$$

$$+ \frac{1}{\Delta y^2} \left[(\boldsymbol{G}_{i,j+3/2}^n)^{(2)} - (\boldsymbol{G}_{i,j+1/2}^n)^{(2)} - (\boldsymbol{G}_{i,j-1/2}^n)^{(2)} + (\boldsymbol{G}_{i,j-3/2}^n)^{(2)} \right] \bigg\}.$$

Different from the one-dimensional case, now we are facing three elliptic equations in each time step. In section 5.2, we will see some simulation results and comparison for these two methods.

References

[1] D.M. Anderson, G.B. McFadden, A.A. Wheeler, Diffuse-interface methods in fluid mechanics, Annu. Rev. Fluid. Mech., 30(1), 139-165 (1998)

[2] D. Armbruster, P. Degond, C. Ringhofer, A Model for the Dynamics of large Queuing Networks and Supply Chains, SIAM J. Appl. Math., 66(3), 896-920 (2006)

[3] N. Bellomo, C. Dogbe, On the modelling crowd dynamics from scaling to hyperbolic macroscopic models, Math. Models Methods Appl. Sci., 18, 1317-1345 (2008)

[4] C. Berthon, M. Breuss, M.O. Titeux, A relaxation scheme for the approximation of the pressureless Euler equations, Numerical Methods for Partial Differential Equations, 22(2), 484-505 (2006)

[5] G.Q. Chen, H. Liu, Formation of delta-shocks and vacuum states in the vanishing pressure limit of solutions to the Euler equations for isentropic fluids, SIAM J. Math. Anal., 34(4), 925-938 (2003)

[6] H. Bijl, P. Wesseling, A unified method for computing incompressible and compressible flows in boundary-fitted coordinates, J. Comput. Phys., 141(2), 153-173 (1998)

[7] A. Chertock, A. Kurganov, Y. Rykov, A new sticky particle method for pressureless gas dynamics, SIAM J. Numer. Anal., 45(6), 2408-2441 (2007)

[8] F. Berthelin, Existence and weak stability for a pressureless model with unilateral constraint, Mathematical Models and Methods in Applied Sciences, 12(2), 249-272 (2002)

[9] F. Berthelin, P. Degond, M. Delitala, M. Rascle, A model for the formation and the evolution of traffic jams, Arch. Rational Mech. Anal., 187, 185-220 (2008)

[10] F. Berthelin, P. Degond, V. Le Blanc, S. Moutari, M. Rascle, J. Royer, A traffic-flow model with constraints for the modeling of traffic jams, Math. Models Methods Appl. Sci., 18, 1269-1298 (2008)

[11] F. Bouchut, On zero pressure gas dynamics, Advances in kinetic theory and computing: selected papers, Ser. Adv. Math. Appl. Sci., 22, 171-190 (1994)

[12] F. Bouchut, Y. Brenier, J. Cortes, J.-F. Ripoll, A hierarchy of models for two-phase flows, J. Nonlinear Sci., 10, 639-660 (2000)

[13] F. Bouchut, S. Jin, X. Li, Numerical Approximations of Pressureless and Isothermal Gas Dynamics, SIAM J. Num. Anal., 41(1), 135-158 (2004)

[14] Y. Brenier, E. Grenier, Sticky particles and scalar conservation laws, SIAM J. Num. Anal., 2317-2328 (1998)

[15] P. Degond, M. Delitala, Modelling and simulation of vehicular traffic jam formation, Kinetic Related Models, 1(2), 279-293 (2009)

[16] P. Degond, S. Jin, J.-G. Liu, Mach-number uniform asymptotic-preserving gauge schemes for compressible flows, Bulletin of the institute of Mathematics, Academia Sinica, 2(4), 851-892 (2007)

[17] P. Degond, L. Navoret, R. Bon, D. Sanchez, Congestion in a Macroscopic Model of Self-driven Particles Modeling Gregariousness, J. Stat. Phys., 138(1-3), 85-125 (2010)

[18] P. Degond, M. Tang, Asymptotic preserving method for the incompressible low mach number limit of the Isentropic Euler equation (2009) (in prep.)

[19] H. Guillard, A. Murrone, On the behavior of upwind schemes in the low mach number limit: II, Godunov type schemes, INRIA research report # 4189 (2001)

[20] H. Guillard, C. Viozat, On the behaviour of upwind schemes in the low Mach number limit, Comput. Fluids, 28(1), 63-86 (1999)

[21] F.H. Harlow, A.A. Amsden, A numerical fluid dynamics calculation method for all flow speeds, J. Comput. Phys., 8(2), 197-213 (1971)

[22] H. Hattori, The Riemann problem for a van der Waals fluid with entropy rate admissibility criterion, Isothermal case, Archive for Rational Mechanics and Analysis, 92(3), 247-263 (1986)

[23] C.W. Hirt, B.D. Nichols, Volume of fluid (VOF) method for the dynamics of free boundaries, J. Comp. Phys., 39(1), 201-225 (1981)

[24] S.Y. Kadioglu, M. Sussman, S. Osher, J.P. Wright, M. Kang, A second order primitive preconditioner for solving all speed multi-phase flows, J. Comput. Phys., 209(2), 477-503 (2005)

[25] R. Klein, Semi-implicit extension of a Godunov-type scheme based on low Mach number asymptotics I: one-dimensional flow, J. Comput. Phys., 121(2), 213–237 (1995)

[26] R.J. LeVeque, The dynamics of pressureless dust clouds and delta waves, J. Hyperbolic Differ. Equ., 1, 315-328 (2004)

[27] R.J. LeVeque, *Finite volume methods for hyperbolic problems.* Cambridge Univ. Press (2002)

[28] X. Li, C. Gu, An all-speed Roe-type scheme and its asymptotic analysis of low Mach number behaviour, J. Comput. Phys., 227(10), 5144-5159 (2008)

[29] P.L. Lions, N. Masmoudi, On a free boundary barotropic model, Annales de l'Institut Henri Poincare/Analyse non lineaire, 16(3), 373-410 (1999)

[30] C.D.Munz, S. Roller, R. Klein, K.J. Geratz, The extension of incompressible flow solvers to the weakly compressible regime, Computers and Fluids, 32(2), 173-196 (2003)

[31] K. Nerinckx, J. Vierendeels, E. Dick, Mach-uniformity through the coupled pressure and temperature correction algorithm, J. Comput. Phys., 206, 597-623 (2005)

[32] S. Osher, R.P. Fedkiw, *Level set methods and dynamic implicit surfaces*, Springer, 2003

[33] S. V. Patankar, Numerical heat transfer and fluid flow, New York: McGraw-Hill, (1980)

[34] P. Rauwoens, J. Vierendeels, E. Dick,, B. Merci, , A conservative discrete compatibility-constraint low-Mach pressure-correction algorithm for time-accurate simulations of variable density flows, J. Comput. Phys., 228(13), 4714-4744 (2009)

[35] M. Tang, Second order all speed method for isentropic Euler equations, in prep.

[36] G. Tryggvason, B. Bunner, A. Esmaeeli, D. Juric, N. Al-Rawahi, W. Tauber, J. Han, S. Nas, Y.-H. Jan, A front-tracking method for the computations of multiphase flow,J. Comp. Phys., 169(2), 708-759 (2001)

[37] E. Turkel, Preconditioning techniques in computational fluid dynamics, Annu. Rev. Fluid Mech., 31, 385-416 (1999)

[38] D.R. van der Heul, C. Vuik, P. Wesseling, A conservative pressure-correction method for flow at all speeds, Comput. Fluids, 32(8), 1113-1132 (2003)

[39] C. Wall, C.D. Pierce, P. Moin, A Semi-implicit Method for Resolution of Acoustic Waves in Low Mach Number Flows, J. Comput. Phys., 181(2), 545-563 (2002),